CHARACTERISTICS OF HIGH RELIABILITY TEPC FOR LONG TERM SPACE MISSIONS

A Dissertation

by

RICARDO DE JESUS

Submitted to the Office of Graduate and Professional Studies of
Texas A&M University
in partial fulfillment of the requirements for the degree of

DOCTOR OF PHILOSOPHY

Chair of Committee,	Leslie A. Braby
Committee Members,	John R. Ford
	Delia Perez-Nunez
	Rainer Fink
Head of Department,	Yassin A. Hassan

August 2018

Major Subject: Nuclear Engineering

ABSTRACT

The Tissue Equivalent Proportional Counters (TEPC) have become a major part of the dosimetry system used on the International Space Station (ISS). TEPCs provide near real-time measurements of absorbed dose and dose equivalent in different parts of the ISS. The current TEPC model used at ISS uses two spherical tissue equivalent proportional counters with their charge sensitive preamplifiers encased in an aluminum vacuum chambers filled with propane gas at low pressure. Both detectors operate at low pressure that simulates a site size of 2 μm in tissue. This site diameter is used because of extensive experience with similar detectors used in industrial applications for mixed field, neutron and gamma, dosimetry. One concern limiting proposals to use TEPCs for dosimetry on manned missions beyond low earth orbit has been the potential for vacuum leaks which result in gradual degradation of proportional counter performance. The potential for leakage can be eliminated by filling the detector with counter gas at atmospheric pressure. This results in a simulated site size of approximately 68 μm for a 3.8 cm detector or 32 μm for a 1.8 cm detector.

Many of the secondary protons produced by neutrons have ranges of as little as 10 μm so TEPCs simulating sites larger than 2 μm may underestimate the dose equivalent in some situations. The ranges of nearly all of the charged particles in space are hundreds of micrometers or more, so dose equivalent can be evaluated using much larger simulated site sizes.

Monte Carlo calculations were used to evaluate the behavior of two TEPCs, 3.8 cm and 1.8 cm diameter. The source particles used were proton, helium, and iron ions. Two different simulations were run for each particle; 1000 MeV/n and the Badhwar-O'Neill flux model distribution. The results show that both detectors operating at atmospheric pressure can estimate dose equivalent in space; the results are essentially identical to those produced by a 2 μm site in the space radiation environment.

DEDICATION

I would like to thank my wife Judith and my two daughters Kelsey and Brianna for their continued support and patience throughout my life and particularly during this chapter of our life.

ACKNOWLEDGEMENTS

I would like to thank my committee chair, Dr. Braby, for his guidance throughout the course of my research. I would also like to thank the members of my committee, Dr. Ford, Dr. Perez-Nunez, and Dr. Fink for their assistance throughout my research.

Thanks also go to my friends and colleagues and the department faculty and staff for making my time at Texas A&M University a great experience.

CONTRIBUTORS AND FUNDING SOURCES

Contributors

This work was supervised by a dissertation committee consisting of Professor Leslie A. Braby, Chair, Professor John R. Ford, advisor, and Dr. Delia Perez-Nunez of the Department of Nuclear Engineering and Professor Rainer Fink of the Department of Biomedical Engineering.

All work for the dissertation was completed by the student, under the advisement of Dr. Leslie A. Braby of the Department of Nuclear Engineering.

Funding Sources

Graduate study was supported by a fellowship from the United States Air Force. The views expressed in this dissertation are those of the author and do not reflect the official policy or position of the United States Air Force, Department of Defense, or the U.S. Government.

TABLE OF CONTENTS

Page

LIST OF FIGURES

Page

LIST OF TABLES

Page

CHAPTER I

INTRODUCTION AND LITERATURE REVIEW

1.1. Objective

A crucial concern to be addressed in preparing for extended human spaceflight missions (Mars mission) is how to keep the crew healthy, safe, and as productive as possible during all phases of the mission. Tissue equivalent proportional counters (TEPCs) provide real-time measurements of absorbed dose and dose equivalent in different parts of the International Space Station (ISS). The current ISS TEPC uses two spherical tissue equivalent proportional counters, 1.2 cm and 3.8 cm in diameter, with their charge sensitive preamplifiers encased in an aluminum vacuum chambers filled with propane gas at low pressure. The challenge is to develop a TEPC that can satisfy the size and power requirements of an extended mission while also providing reliable dosimetry for the complex radiation environment in space, which includes both steady-state galactic cosmic ray (GCR) radiation and highly variable solar particle event (SPE) radiation. Generally a detector design is a compromise between preferred characteristics and practical requirements. The two detectors used at ISS operates at a pressure that simulates a sites 2 μm in diameter. This site diameter is used because of extensive experience with similar detectors used in industrial application for mixed field, neutron and gamma, dosimetry.

The main objective of this research is to determine the characteristics of two highly reliable TEPCs for long term space missions. These proportional counters will be

filled with counter gas at atmospheric pressure in an attempt to eliminate the potential for leakage. Aspects of their performance will be simulated and evaluated by employing microdosimetric techniques. The microdosimetric quantities, dose-mean lineal energy, frequency-mean lineal energy, and the average quality factor will be determined and compare with the same quantities obtained when the detector is operated under low pressure to determine if much larger simulated sites can adequately determine dose equivalent. A knowledge of the gas gain is important to optimize the design and operating characteristics of the detectors. The gas gain will be obtained as a function of voltage to determine the best operating conditions of the detectors.

There are three main goals for this research:

1. Calculate y_D, y_F, and the average quality factor of a 3.8 cm TEPC that operates at atmospheric pressure. This detector is a prototype of the one used at ISS.
2. Calculate y_D, y_F, and the average quality factor of a 1.8 cm TEPC that operates at atmospheric pressure. This detector was designed to meet the stringent space requirements for future deep-space human exploration missions.
3. Determine gas gain of both detectors and evaluate their characteristics to determine the feasibility to measure absorbed dose and equivalent dose in space.

1.2. Space Radiation Environment

As space missions become more technically sophisticated and the focus is toward a Mars mission, they will be more sensitive to space environment, especially charged energetic particles of different origin. The spacecraft systems are vulnerable to space

environment through the influence of energetic charged particle and plasma populations, while aircraft electronics and aircrew are vulnerable to cosmic rays and solar particle events (Miroshnichenko, 2003). About half of the dose equivalent in space is due to high LET radiation which consists of heavy charge particles. They produce various effects such as absorbed dose, lattice displacement damage, and interference with sensors and spacecraft instruments. The main sources of space radiation are Galactic Cosmic Rays (GCR) and Solar Particle Events (SPE).

Galactic cosmic rays (GCR) are charged particles that originate from sources beyond solar system. The GCR spectrum consists of 85% protons, 14% alpha particles, and 1% elements heavier than helium. The highest-intensity GCR is found between a few tenths and a few tens of GEV per nucleon, where the particles can penetrate tens or hundreds of centimeters of shielding. From the point view of space systems it is particles in the range 1-20 GEV per nucleon, which have the most effect. They travel at close to the speed of light and appear to have been travelling through the galaxy for some ten million years before intersecting the Earth (Miroshnichenko, 2003). Galactic cosmic rays also include electrons and positrons, but their intensity are too low to be of practical concern. The GCR flux outside of the solar system is presumed to be constant, but the flux in the solar system and near the Earth depends on the sun conditions. To reach Earth or other planets, GCR must penetrate the heliosphere, the magnetic plasma that surrounds the sun, which suppresses the entry of charged particles from the interplanetary space (National Research Council, 2008). The strength of the interplanetary magnetic field increase with proximity to the sun. This field varies with

the solar activity cycle. The solar cycle is an eleven-year cycle where the sun experience solar maximum and solar minimum referring respectively to periods of maximum and minimum sunspots counts. At a solar maximum, the GCR flux near the Earth will be a minimum since the interplanetary magnetic field is strongest, and at a solar minimum the GCR flux will be a maximum since the interplanetary magnetic field is weak. This solar cycle variation in the strength of the interplanetary magnetic field is most likely due to the changing rate of coronal mass ejections (CMEs) (National Research Council, 2008). The higher rate of CMEs at solar maximum impede cosmic rays access to the inner heliosphere by increasing the level of magnetic turbulence (National Research Council, 2008). Near solar minimum, in the absence of many CMEs and their corresponding magnetic fields, GCR particles have easier access to Earth. As the solar cycle follows a roughly 11-year cycle (estimated 7 years solar maximum and 4 years solar minimum), the GCR will follow the same pattern. But unlike the solar cycle, where burst of activity can change the environment quickly, the GCR spectrum remains relatively constant in energy and composition, varying only slowly with time.

Life on the Earth's surface is protected from GCRs by many factors. One of the many factors is the magnetic field that fills the solar system, which is commonly referred as heliospheric magnetic field. The Earth's magnetic field also acts to deflect cosmic rays from its surface. The magnetic field deflects the cosmic rays toward the poles where their intersection with the atmosphere forms what we know as the aurorae. The Earth's atmosphere is resistant to primary cosmic rays with energies below about 1 GeV/n, therefore only secondary radiation can reach the surface. This secondary

radiation is absorbed in the atmosphere and attenuated by radioactive decay in flight of some particles such as muons. It has been estimated that the world's population receives an average of 0.4 mSv of cosmic radiation annually (not including radiation from naturally occurring radioactive material) due to atmospheric shielding (Health Threat, 2015). The radiation increases as the altitude increases and it is at its higher at the Polar Regions. As a result of this protection from solar radiation to Earth's surface, the energy input of GCRs to the surface is negligible, roughly about 10^{-9} of solar radiation above atmosphere. Unfortunately for deep space long term missions, astronauts are not protected by the Earth's magnetic field and atmosphere and therefore may experience a great radiation risk. A risk that will depend on how long the mission is and how far they travel in deep space.

Solar Particle Events (SPE) are cosmic rays of solar origin. These are energetic particles, some with energies exceeding several GeV, accelerated in sporadic events at the sun during solar activity. SPEs occur intermittently throughout the solar cycle, although much less frequently near solar minimum. In comparison with GCR, SPE events are the most dangerous components of radiation environment, due to serious difficulties in the prediction of those events. On the other hand, because of SPE low average energy relative to GCR, they can be controlled by shielding. In addition to the particles, signatures of SPEs also include significant increases in solar radio emissions, x-rays, and detectable levels of gamma rays and neutrons from the sun. However the ratios of these signals is highly variable between SPE. Due to this uncertainty in the occurrence of SPE, extensive research took place in the 1980s that led to the

classification of SPE into two types, “gradual” and “impulsive”. In gradual SPEs shocks driven by fast CMEs are the dominant accelerator. The particle acceleration in impulsive SPEs are believed to be due to magnetic reconnection processes similar to those that go on in solar flares (National Research Council, 2008). In comparison with gradual SPEs, impulsive SPEs are characterized by small intensities, low energies that do not penetrate typical shielding, short durations, and distinctive patterns of enhancements in heavy ions. In other words, impulsive SPEs are not a radiation hazard to astronauts because of their low particle fluxes. On the other hand, gradual SPEs are a radiation hazard to astronauts because of their large intensities. Therefore, for the purpose of this research the main concern for astronaut safety are the gradual SPEs. The particles have ranges in water from millimeters up to tens of centimeters and they can increase in intensity within minutes to tens of minutes of the onset of solar activity. The flux during the first few minutes is not isotropic and eventually becomes isotropic within hours depending on particle energy. The maximum flux could occur minutes to days after onset, also depending on energy. Some of the largest SPEs are part of different event episodes, produced as a single solar active region rotates across the face of the sun. These episodes are unpredicted and could constrain space operations for various days. These increases are referred to as energetic storm particles (ESP) events (National Research Council, 2008). These unpredicted rare events are the most hazardous radiation environment to which astronauts may be exposed.

In general, protons comprise more than 90% of the energetic ions produced in an SPE. Data obtained from Dotson et al. (1975) and Sladkova et al. (1998) contain data of

all flux increases that have been recorded near Earth for protons with energies greater than 10 MeV (Miroshnichenko, 2003). The source of these protons are not always identified with the solar flares, sometimes they may be due to particles accelerated by shock waves driven into interplanetary space by large CMEs. Protons are the primary concern when evaluating SPE radiation hazards but because the same process that accelerates protons to high energies also accelerates heavier ions, they have to be considered as well. It is important to assess whether solar heavy ions might pose a threat to astronaut safety. Heavier ions must have higher initial energies in order to penetrate a typical shielding. Given that SPE fluence at the skin of the spacecraft fall steeply with increasing energy, the higher-penetration thresholds should be sufficient to minimize the dose from solar heavy ions (National Research Council, 2008).

According to the National Research Council there are more than 40 years of solar particle events observations. These data have been very useful in the design of spacecraft shielding for the protection of the astronaut crew and the spacecraft equipment.

1.3. Experimental Microdosimetry

Experimental microdosimetry is a method that measures the absorbed dose in an event by event manner inside a tissue equivalent volume with site diameter of the order of micrometers. The term microdosimetry originated when Rossi and colleagues (1955) developed a conceptual framework with experimental methods for the analysis of the microscopic distribution of absorbed energy in irradiated matter (ICRU, 1983). The

absorbed dose and the number of energy deposits with their magnitude and spatial distribution are expected to influence the effect of the radiation on biological structures. Furthermore by determining the size and distribution of energy deposit, valuable information can be obtained on the different effects for the same absorbed dose. This has been found useful for the study of the biological effects and it is well defined in the term relative biological effectiveness (RBE) for different radiation types.

The tissue equivalent proportional counter (TEPC) is a widely known instrument used for experimental microdosimetry. This instrument is describe in detail later in this paper. TEPCs can provide a direct reading of the absorbed dose by measuring the individual energy deposition events of secondary radiations produced by neutron and gamma rays. The spectrum recorded during the measurement can be utilized to analyze the radiation field. The analysis of this radiation field will help to determine the dose contributions by different types of particles, components of unknown radiation fields, and understand of the radiation effects on biological structures.

The first experiments on microdosimetry were based on the concept of sites that are regions of specified size and dimensions in which the energy absorbed from ionization radiations is considered without regard to its microscopic distribution within a site (Rossi and Zaider, 1996). This approach was called regional microdosimetry and continues to be studied today because it involves quantities that can be related to radiation effects. A more advanced study was later developed by Kellerer which was called structural microdosimetry (Rossi and Zaider, 1996). Structural microdosimetry is a detailed description of the microscopic pattern of energy absorption and it is essential

to determine the sensitive components in irradiated matter. The fundamental work of Rossi in 1955 with low pressure proportional counters (LPPC) was intended to measure LET and evaluate RBE. He was not able to measure LET using low pressure proportional counter, a spherical chamber of 2 cm diameter filled with low pressure gas to simulate a 1μm tissue site, but realized that the quantity measured might be more relevant to RBE. When using these counters Rossi discovered that the measured data represented the energy distributions needed to determine the effect of the radiation on a cell (Kellerer, 2002).

The ICRU Report 16 (ICRU, 1970) described material on LET distributions and mean values for a wide range of radiations and stated the advantages of microdosimetry. ICRU Report 19 (1971) defined some microdosimetric quantities and distributions. These reports were replaced by Report 36 (1983) which also included definitions of microdosimetric quantities and distributions. Report 36 quantities are the base of this research and are described in this section. Microdosimetric concepts were also employed in ICRU report 26 (1977) which also deals with specific problems of neutron dosimetry in radiobiology and radiotherapy.

The elementary quantity in microdosimetry studies is the energy deposited ε_i. The energy deposited ε_i is a single interaction i defined as:

$$\varepsilon_i = T_{in} - T_{out} + Q \qquad (1.1)$$

Where T_{in} is the energy of the incident ionizing particle (exclusive of rest mass), T_{out} is the sum of the energies of all ionizing particles leaving the interaction (exclusive of rest mass), and Q is the changes of the rest mass energy of the atom and all particles involved in the interaction. The unit of ε_i is the joule (J) and may also be expressed in the unit eV. The energy imparted ε_i may be considered as the energy deposited at the point of interaction, if quantum mechanical uncertainties and collective effects are neglected (ICRU, 1983).

The energy imparted, ε, to the matter in a volume is:

$$\varepsilon = \Sigma \varepsilon_i \tag{1.2}$$

The summation is performed over all energy deposits, ε_i, in that volume. The unit of ε is also joule (J) and has a random behavior which indicates the stochastic nature of imparted energy.

The specific energy, z, is the quotient of the energy imparted, ε, by ionization radiation to matter of mass m:

$$Z = \varepsilon / m \tag{1.3}$$

The unit of z is the joule per kilogram (J/kg) which is also expressed in Gray (Gy).

The lineal energy, y, is the quotient of the imparted energy, ε, by $\bar{l}$, the mean chord length in that volume:

$$y = \varepsilon / \bar{l} \tag{1.4}$$

The unit of lineal energy, y, is the joule per meter, but the unit mostly used is the keV/μm. The mean chord length is the mean length of randomly oriented chords in that volume. For a spherical detector, the mean chord length $\bar{l}$ = 2/3 *d, where d is the diameter of the simulated site size. This formula is derived from a convex body where $\bar{l}$ = 4V/a, where V ($V = \pi d^3/6$) is the sphere volume and a ($a = \pi d^2$) is the surface area of the body.

The lineal energy is a stochastic quantity. When particles interact with a given volume, they can release, with different probabilities, different quantities of energy which generate a broad spectrum of lineal energy. The value of the distribution function, F(y), is the probability that the lineal energy is equal to or less than y. The probability density f(y) is the derivative of F(y) with respect to y:

$$f(y) = dF(y) / dy \tag{1.5}$$

This is known as the lineal energy distribution. The lineal energy distribution, f(y), is independent of the absorbed dose or dose rate. The mean value of f(y) is defined by the following equation:

$$\bar{y}_F = \int yf(y)\, dy \tag{1.6}$$

This is called frequency-mean lineal energy and is a non-stochastic quantity. The dose distribution, d(y), can be determined from the above distribution and is the normalized distribution of the product yf(y) which represents the relative contribution of events with magnitude y to the dose. Let D(y) be the fraction of absorbed dose delivered with lineal energy less than or equal to y, then the dose probability density, d(y), is the derivative of D(y) with respect to y:

$$d(y) = d\,D(y) / dy \tag{1.7}$$

Since the distribution d(y) is independent of the absorbed dose or dose rate, the expected value is:

$$\bar{y}_D = \int y d(y)\, dy \tag{1.8}$$

and is called dose-mean lineal energy. $\bar{y}_D$ is also a non-stochastic quantity. The relationship between d(y) and f(y) and between $\bar{y}_D$ and $\bar{y}_F$ is:

$$\bar{y}_D = (1 / \bar{y}_F) \int y^2 d(y)\, dy \tag{1.9}$$

1.4. Previous work

Tissue-equivalent proportional counters (TEPC) are being continuously used on the International Space Station (ISS) to measure low-Earth orbit radiation doses that

space crews are exposed to while living and working on the space station (Riman, 2012). But long before the International Space Station was build, astronaut have been exposed to space radiation during the Mercury and Space Shuttle missions. The first Mercury missions did not have dosimeters because of low probability, low exposure to astronauts, but not long after the Mercury-Atlas 7 mission, radiation was detected and Thermo-luminescent (TLD) dosimeters were added to the astronaut's suit and located around the aircraft (Perez-Nunez, 2008). For the last two Mercury missions the radiation received by the astronauts was much less than the actual annual dose limit of 50 mSv for a radiation worker. NASA continued monitoring their astronauts' radiation exposure for the Gemini, Skylab, Apollo, and Space Shuttle missions. Astronauts have been classified as radiation workers and therefore a program was implemented to protect them from excessive radiation exposure. They have been provided with passive dosimeters for personal detection and radiation survey meters to quantify radiation at various locations in the spacecraft.

Since the Mercury program, the doses received by the astronauts have increased but they were still below the limits for a radiation worker. The main concern for the ISS astronauts is their long duration missions, compared with Mercury and Skylab astronauts they have been much longer and the typical dose is more than double. The first routine use of a TEPC on ISS was Expedition 2 in 2001. TEPCs collect data as a function of time to measure the dose and estimate the dose equivalent by making spectral measurements of the energy loss of the radiation as it passes through the detector volume. The crew was able to read the current level through an electronic display and

had the capability to telemeter data to the ground every 10 seconds. This TEPC operated successfully for 5 years and several improved versions were used on ISS through 2011. These detectors were of cylindrical shape with field tubes to achieve good energy resolution and minimum sensitivity to noise created by vibration. The inside diameters of these detectors is 5.1 cm. The new version used on board ISS is part of the next generation TEPC which uses a multi-detector arrangement and a laminated spherical detector design to provide isotropic response and extended dose rate range. The main challenge when the spherical detectors were designed was to create a uniform electric field along the axis of the detector. Since the distance between the spherical shell (cathode) and the anode wire placed along the diameter of the sphere is not constant, the electric field will be stronger and the gas gain higher near the ends of the anode. This means the gas gain will not be constant throughout the detector. The approach used to correct this problem was to divide the cathode in several rings with different thicknesses and adjust the potential difference between each ring and anode to produce a constant electric field along the length of the anode. The new design used for the ISS are two detectors; one is a 3.8 cm diameter detector divided into 11 rings with 5% voltage increments and the other is a 1.25 cm diameter detector divided into 9 rings (Perez-Nunez, 2011). Each detector is filled with propane gas at low-pressure to simulate 2 µm. These detectors were developed at Texas A&M and were adapted to meet mechanical and electronics parts' specifications for flight hardware at Johnson Space Center (JSC).

1.5 Statement of the Problem

The TEPC prototype has been developed to measure the dose at a tissue depth of about 5 mm due to high-energy electrons and protons produced during solar particle events and galactic cosmic rays. This design has been used extensively in the International Space Station (ISS) to monitor the dose and equivalent dose to astronauts while working in space. What is not entirely clear, however, is the use of TEPCs for dosimetry in missions beyond low-earth orbit due to the potential for vacuum leaks which result in gradual degradation of proportional counter performance. This is a great uncertainty and risk for astronauts that will be in long missions such as the Mars mission which could take 5 years or more in deep space. They have to depend on a TEPC that does not requires refilling the gas in a continuous basis. What is proposed in this research is to fill the TEPCs with counter gas at atmospheric pressure to eliminate the potential for leaking. This results in a simulated site size of 68 μm for the 3.8 cm diameter detector and of 32 μm for the smaller and more compact 1.8 cm diameter detector. The objective is to determine if these site diameters will work well for evaluation of absorbed dose and dose equivalent in space. A 2 μm site diameter has been used because of extensive experience with similar detectors used in industrial applications for mixed field, neutron and gamma dosimetry. In the industrial mixed field application many of the secondary protons produced by neutrons have ranges of as little as 10 μm, therefore TEPCs simulating sites larger than 2 μm may underestimate mean quality factor and therefore the dose equivalent. In space because of GCRs and SPEs the

range of charge particles is much larger, in the hundreds of micrometers or more, dose equivalent can be evaluated using much larger simulated sizes.

When designing TEPCs for deep-space mission, there are some stringent requirements, established by NASA, which need to be met before the detector can be operational. Key characteristics include small mass because of space constraint and low power consumption. One approach to the design of a compact, highly reliable, dosimeter is to use several small, possibly 1.8 cm diameter, proportional counters operating at atmospheric pressure to provide the same cross sectional area, and therefore the same radiation sensitivity, as a 3.8 cm diameter detector. The first step in determining the feasibility of this approach is to determine the gas gain of the proposed proportional counter at atmospheric pressure. The sensitivity to neutrons of the two detectors at low and atmospheric pressure will be measured and the response to GCR particles will be calculated to establish the use of the detectors at atmospheric pressure. The quantities of interest will be the dose-mean lineal energy $\bar{y}_D$, frequency-mean lineal energy $\bar{y}_F$, and the average quality factor Q. These are quantities related to the biological effects of space radiation and are essential for the radiation protection of astronauts in deep-space missions.

CHAPTER II

RADIATION DOSIMETRY

2.1. Stopping Power and Linear Energy Transfer

Any charged particle passing through matter loses energy to the electrons of the atoms it encounters. Energy is transferred between charged particles by coulomb-force interactions, causing the affected electrons to move into higher orbital energy levels (excitation) or to be ejected from the orbit (ionization). Each free electron may then produce additional ionization or excitation by interacting with other atoms until its energy is expended. The rate of kinetic energy loss increases per collision as the energy of the particle decrease until the remaining energy is not enough to produce additional ionization or excitations.

The average energy loss per unit path length as the particle traverses the medium is known as the stopping power. There are two components to the stopping power for a charged particle; the collision stopping power, which represents the result of ionizations and excitations, and the radiative stopping power, which is the result of photon emission associated with bremsstrahlung (Rossi & Zaider, 1996). The rate of energy loss with distance traversed is known as the stopping power of the material and is given by:

$$dE / dX = [\, 2e^4 z^2 N_A Z \,] B / mv^2 \qquad (2.1)$$

Where N_A is the Avogadro's number (6.022×10^{23} atoms per mole) and A is the atomic mass of the target atom. Z and v are the charge number (1 for electron) and velocity of the incident particle, respectively. B is the material's mass stopping power and depends on the energy:

$$B = Z [\ln (2mv^2/I) - \ln (1-v^2/c^2) - v^2/c^2] \quad (2.2)$$

The mean excitation energy I, is the average excitation and ionization potential of the absorber and is a determined parameter for each element. The equation above defines mass stopping power which is often expressed in units of energy lost per unit mass thickness, measured along the particle path in MeV $cm^2 g^{-1}$. If a substance is compared in gaseous and solid form, then the linear stopping powers of the two states are very different just because of the different density. When you multiply the mass stopping power by the density, then you obtained the linear stopping power in MeV cm^{-1} which can also be expressed as KeV μm^{-1} for unit density material.

The stopping power for any element can be illustrated by the Bragg's curve as seen on Figure 2.1. For an element or compound, the mass collision stopping power is the sum of the mass collision powers of the atomic constituents weighted by the fractional contribution by weight of each constituent (Rossi & Zaider, 1996). Due to the effect of straggling, the Bragg curves for individual identical particles will differ. When a charged particle moves through matter, it ionizes atoms of the material and deposits its energy in the medium. The peak seen in figure 2.1 is called the Bragg peak. This peak

occurs because the charged particle interaction cross section increases as its energy decreases. Energy lost by charged particles is inversely proportional to the square of the velocity, which causes the peak occurring before the particle comes to a complete stop.

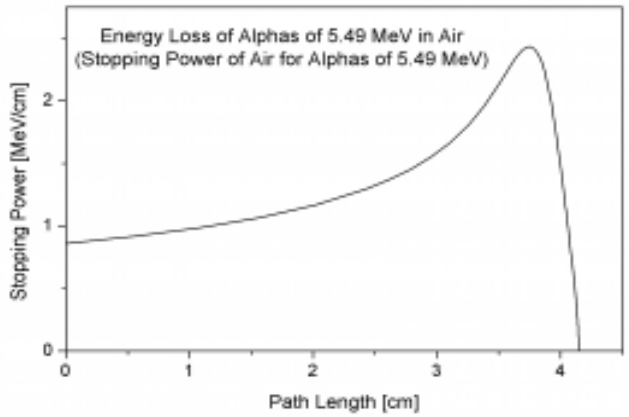

Figure 2.1 Bragg curve of 5.49 MeV of alpha particles in air. Reprinted with permission from Paul, 2015.

The continuous slowing-down approximation (CSDA) is a very close approximation to the average path length traveled by a charge particle as it slows down to rest. It can be calculated by integrating the reciprocal stopping power over energy:

$$\Delta x = \int_0^{E_0} dE/S(E) \tag{2.3}$$

Where Δx is the range, S(E) is the linear stopping power, and E_0 is the initial kinetic energy of the particle. The range of charged particles of a given energy is a unique quantity in a specific absorber material. Knowing the particle range is extremely

important when designing radiation dosimeters. When determining the wall thickness of the detector, the range of secondary charged particles is an important factor to know because the wall thickness must be greater than the range of that particle in order to provide secondary particle equilibrium (SPE) in the detector material. SPE is needed for some measurements of indirectly ionizing radiation but is generally not a problem for charged particles such as GCR and SPE. The International Commission on Radiation Units and Measurements (ICRU) Report 49 includes a list of stopping powers and ranges for 73 materials and covers the energy ranges 1 KeV to 10,000 MeV for protons and up to 1000 MeV (250 MeV/n) for alpha particles (Arshak & Korostynska, 2006). Shown in Figure 2.2 is the stopping power for alpha particles in A-150 tissue-equivalent plastic material. The A-150 is the tissue-equivalent (TE) plastic material used in this detector and will be discuss in detail later on this paper.

The graph shown on figure 2.2 is very helpful to quickly look up the information on stopping power, but in order to generate the desired data for all the energy ranges, the National Institute of Standards and Technology (NIST) Physics Laboratory (https://physics.nist.gov/cgi-bin/Star/ap_table.pl) developed web databases to generate stopping powers and ranges for protons and helium ions tabulated in ICRU report 49.

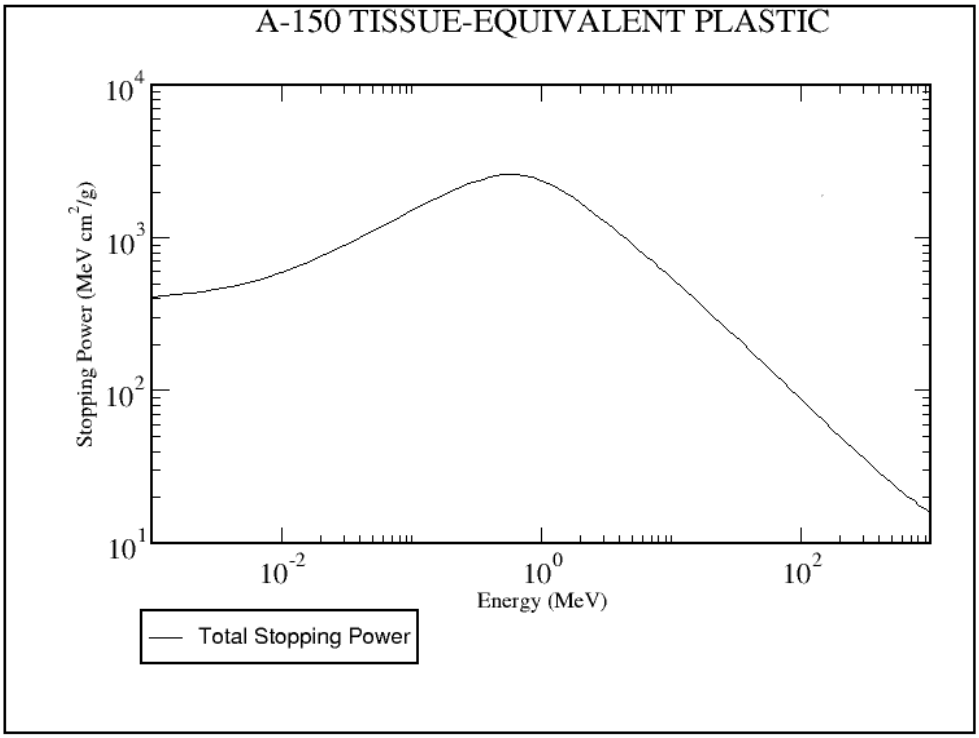

Figure 2.2. Stopping power for alpha particles in A-150 TE plastic. Reprinted with permission from Berger et al., 2017.

Stopping power is closely related to linear energy transfer (LET), since both equal the energy loss. But the stopping power and LET concepts are different in terms of components of stopping power which are not contained in LET. Radiobiologist and Medical physicist usually use the term LET and Nuclear Engineers or non-medical physicist use the term stopping power. The unrestricted LET$_\infty$ is defined as the energy transferred per unit length of the track, the collision stopping power. It is usually expressed in kiloelectron volt per micrometer (keV/μm). Damage to biological tissue by ionization radiations is caused by energy absorption in the biological microstructures. This transfer of energy to the nucleus can result in biological changes to cells or cell

components. LET is an average quantity because at the microscopic level, the energy per unit length of track varies over a wide range (Hall, 2012). The LET is very useful to indicate the quality factor for different types of radiation. For a given type of charged particle, the higher the energy, the lower the LET and therefore the lower its biologic effectiveness. Thus, the higher the LET, the higher its biological effectiveness.

2.2 Dosimetry

The operation of any radiation detector depends on the manner in which the incident radiation interacts with the material of the detector. It is important to understand the process and mechanism by which radiations interact and lose their energy in matter. Radiation dosimetry is the process of determining the energy absorbed in a specified target from a radiation field (Arshak & Korostynska, 2006). The process by which the energy is absorbed in a target depends on the radiation type and the energy. There are two ways by which we can detect the incident radiation in the medium, either by ionization directly or by secondary radiation (indirectly) which emits a particle that produces ionization in the medium. For this research we are more concerned with the detection of directly ionizing GCR and SPE particles and secondarily with neutrons which when interacting with the medium will produce a secondary particle that will be detected by one of an increasing variety of detectors discussed later in this section.

In the field of Health Physics, radiation dosimetry is useful for the measurement, calculation, and assessment of the radiation dose absorbed by the human body. The total absorbed dose to the human body includes both internal and external exposure. Internal

exposure is due to ingested or inhaled radioactive materials, and external exposure is due to irradiation by sources of radiation. Dosimetry is used for radiation protection of occupational radiation workers in a routine basis. Astronauts working on space, are monitored continuously by passive and active dosimeters to make sure they do not go over the annual established NASA radiation limits. The annual limit for a radiation worker in industry is 5 Rem (50 mSv). NASA exposure limits varies with the age and sex of the astronaut. Mission risks vary over the approximately 11-year solar cycle, with higher GCR doses at solar minimum and higher likelihood of SPEs near solar minimum. Radiation limits for astronauts could be anywhere from 440 mSv for a 30 years old female to 900 mSv for a 60 years old male. This is based on NASA Space Radiation Cancer Risk Model to perform Risk of Exposure Induced-Death (REID) assessment for astronauts. The most current model and tables with the radiation limits by age and sex can be found in NASA Space Flight Human Standard Volume 1 (NASA, 2015). The passive dosimetry corresponds to the use of a dosimeter, where certain physical characteristics are modified by the incident radiation (Arshak & Korostynska, 2006). The measured dose is usually taken as an estimate for the effective dose which is recorded and reported after evaluation. This types of dosimeters are called “passive” because they do not provide direct readouts and can operate without any active means. Thermo-Luminescent Dosimeters (TLDs), Optical Stimulated Luminescences (OSLs), and radiological films are some of the devices used as passive dosimeters. Active dosimetry can provide real time information about radiation dose and dose rate. The active dosimeters are electronic portable instruments that provides a direct display of the

accumulated dose and may also have some additional functions such as alarm threshold settings for dose or dose rate values. Many also provide an audio and visual alarm to alert the user when they are entering a high radiation field. These dosimeters are used for complimentary dosimetry in the case of a high radiation field. Some examples of active dosimeters are ionization chambers and Geiger counters (GM). Active dosimeters are generally more convenient than passive dosimeters because you get real time instant information. Passive dosimeters are inherently of the integrating type (e.g. TLDs), while active dosimeters can measure both integral and differential modes (ionization chambers).

2.2.1 Calibration

Some uses of radiation dosimetry have critical requirements for accurate dosimetry, because they are directly related to health and safety. The dosimetry accuracy required for radiation protection purposes is somewhat less compared to radiation therapy; nevertheless, accurate dosimetry is also required for the protection of human lives. Most dosimeters exhibit dose response that is dependent on the energy of the radiation measured, so corrections are always applied to the readings of dosimeters and survey meters to determine the required dosimetric quantity. In measuring the absorbed dose to the human body, dose measurement is usually calculated and calibrated as dose to water. This can be done because the human body is approximately 70% water and has an overall density close to 1 g/cm^3. Calibration is the set of operations that under specified conditions establish the relationships between values indicated by a

measuring instrument or values represented by a material measure and the corresponding known values of a measurement (Arshak & Korostynska, 2006). For some detectors a few experimental tests have to take place to determine a calibration factor. Calibration factors are used as a reference for the follow on experimental test taken under the same parameters. Neutron dosimeters are usually calibrated using specific neutron sources (AmBe or CF) and calibration factors are established for this individual dosimeter. Only a few dosimeters exhibit a linear relationship between the signal and absorbed dose. Therefore, for most types, it is not possible to define a single calibration factor for a dosimeter, and a nonlinear calibration function has to be used instead.

2.2.2 Gas-filled Detectors

One of the major results of the interaction of radiation with matter is the creation of ions. In a gas-filled detector the radiation interacts with gas atoms to produce ions which can be collected as an electrical charge or current. Gas-filled detectors consist of a cylindrical or spherical cathode with a window, an axial anode, and a sensitive volume of gas. The detector may be sealed to contain the gas, the gas may be continuously replenished giving a flow through the detector or the detector can be open to ambient air. The ion pair consist of; two particles, the positive ion and an electron. The detection of the production of ion pairs in the gas is the basis upon which gas detectors operate. Consider this simple view in figure 2.3. Here we have two electrodes with the gas between them. A DC voltage is placed between the electrodes, resulting in the electrons moving towards the positive electrode and the ion moving towards the negative

electrode. When a high enough voltage is applied, gas multiplication occurs close to the anode wire where electrons multiply creating an avalanche. The gain of this process is defined as the number of electrons collected on the anode wire for each primary electron produced in the original ionizing event.

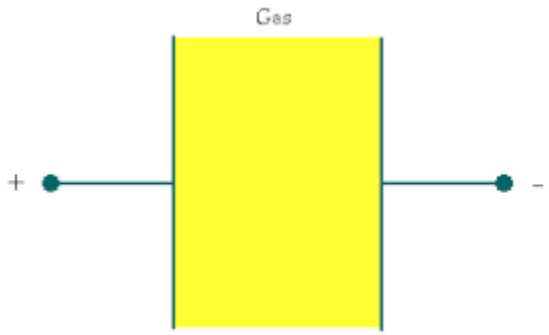

Figure 2.3. Gas-filled detector basic operation. Reprinted from Saha, 2012.

The differences between various types of detectors operated in pulse mode depends on the potential applied to the anode. The detector can work as an ionization chamber, proportional counter, or Geiger counter depending on the voltage applied. The voltage in an ionization chamber is high enough to prevent electrons from recombining but not high enough for gas multiplication. In proportional counters, the voltage is high enough for gas multiplication. Each electron produced by the initial ion pair causes one avalanche. Since the gas multiplication will be linear, the charge collected will be proportional to the number or original ions pairs created. In Geiger counter the voltage is increased still further until the gas multiplication reaches saturation. In this region the

output pulse from the detector is of the same amplitude and no longer reflects any properties of the incident radiation.

2.3 Tissue Equivalent Proportional Counter (TEPC)

The TEPC was developed by Rossi and Rosenzweig in 1956. The counter produces pulses with amplitudes that are proportional to the energy deposition of secondary charged particles generated in the tissue-equivalent plastic wall and the tissue equivalent gas used to fill the device. Analysis of the pulse height distribution produced by this counter demonstrated that the portions of the distribution produced by electrons and protons could be distinguished, so the total dose measured with the TEPC would yield a measurement of both the gamma and neutron dose. Since the initial TEPC was developed, several variations of the basic design have been developed, but the basic operational principles have not changed.

The TEPC is a type of proportional counter whose walls and fill gas mixture mimic the elemental composition of biological tissue (Knoll, 2010). It is a type of gas-filled detector that almost always operates in pulse mode and relies on the phenomenon of gas multiplication to amplify the charge represented by the original ion pairs created within the gas. Simulation of microscopic regions in solids by geometrically similar gas volumes of equal effective dimensions avoids the problem of determining energy absorption in micrometer sized volumes (Rossi & Zaider, 1996). The applicability of proportional counters has been expanded because the variance-covariance method permits determination of quality factor of higher dose rates and in the pulsed fields of

accelerators, while multi-element counters as tested by Rossi can extend the applicability of tissue-equivalent (TE) counters to the low-dose rates that are encountered in neutron measurements (Rossi & Zaider, 1996). External radiation fields produce broad energy spectra of charged secondaries in TE proportional counters, and these secondaries, in turn, deposit largely different energies in the counter. As a result the microdosimetric spectra provides the characteristic information to determine the quality of the radiation field (ICRU, 1986).

Design considerations to keep in mind when designing a TEPC based dosimeter are cost, size, ease of construction, power consumption, weight, and real time display of data. Ease of construction is related to detector design because the design can limit which parts can be constructed. Cylindrical detectors are the easier to design and construct, but their chord length distribution is more complicated than that of a spherical detector and their response is not isotropic (Braby et al., 1995). The spherical detector are preferred for most application because the response is isotropic. Other design considerations are wall material, vacuum chamber, and gas gain. The wall material most commonly use is the A-150 tissue-equivalent plastic. The thickness of the wall provides sufficient buildup of delta rays into the spherical gas cavity. The vacuum chamber provides reliable electromagnetic shielding. The gas gain should be uniform through the detector to allow the particles that deposit equal energies in the gas to produce the same avalanche. In the spherical detector designed by Rossi's group, this was done by adding a helical grid around the anode. In detectors following the design devised by Benjamin, fields shaping electrodes are used to reduce the field at the ends of the anode. In the

detectors currently in use on the space station this was done by dividing the cathode (spherical shell) into several rings with different thicknesses, and adjusting the potential difference between each ring and the anode to produce an electric field that is constant along the length of the anode.

The gas gain, G, can be defined as the average number of electrons collected at the anode per electron liberated by the charged particle track. Two important factors that determine gas gain are the electric field strength and gas pressure of the sensitive volume of the counter. Proportional counters operations is based on the exponential growth of the electron avalanche (Rossi & Zaider, 1996):

$$G = N/N_o = e^{\alpha d} \qquad (2.4)$$

Where G is the gain, N is the number of electrons resulting from multiplication, N_o the initial number, and α is the towsend coefficient approximated by:

$$\alpha / p = Ae^{-Bp/E} \qquad (2.5)$$

Where p is the pressure of the gas, E is the electric field strength and A and B are constants determined to be 10 cm^{-1} $torr^{-1}$ and 210 V cm^{-1} $torr^{-1}$ respectively (e.g. methane based TE gas) (Rossi & Zaider, 1996).

The electric field for a cylindrical detector at radius r is given by:

$$E = V / r \{\ln(c/a)\} \quad (2.6)$$

Where V is the voltage applied between the cathode and anode, c is the cathode radius and a is the anode radius.

The electric field strength increases as r decreases and reaches a value sufficient for gas multiplication near the anode wire. Therefore gas multiplication does not depend on the position of formation of the primary ions, thus the resulting pulse will be proportional to the number of primary ions. The gas gain applications for this research will be discussed in details in section 4.1.2.

2.4 Gas Pressure

The pressure of a gas is the force that the gas exerts on the walls of the container. An important property of any gas is its pressure. A gas is composed of a large number of molecules that are very small relative to the distance between molecules. These molecules are in constant motion and they collide with each other randomly (NASA Glenn Research Center, 2015). Each molecule has mass, momentum, and energy. The density of the gas is the sum of the mass of the molecule divide by the volume which the gas occupies. The pressure of the gas is simply the measure of the linear momentum of the molecules. In other words, as the molecules collide with the walls of the container, the force produced by this momentum can be measured. Pressure is defined by:

$$P = F / A \quad (2.7)$$

Where P is pressure, F is force, and A is the area. The temperature is a big factor in the molecules movement and behavior, therefore the temperature of a gas is a measure of the mean kinetic energy of the gas. The molecules are in constant random motion and the higher the temperature, the greater the motion.

When we are dealing with very large number of molecules that are in random motion and moving in any direction, the whole gas does not appear to be moving, but in fact the individual molecules are in constant motion. If the gas is enclosed in a container, a pressure is detected on the walls of the container. This pressure is the result of the molecules colliding with the walls of the container. We can make the container smaller down to an infinitely small point, and the pressure has a single value at that point. Therefore, pressure is a scalar non-stochastic quantity, not a vector quantity. Pressure acts in all directions at a point inside a gas (NASA Glenn Research Center, 2015).

The purity of the gas is a very important factor for the performance of a proportional counter. It is necessary that the gas have the correct atomic composition and avoid the contamination of the gas by electronegative gases such as oxygen (Rossi & Zaider, 2006). The fill gas in proportional counters must be chosen from those gases that do not exhibit an appreciable electron attachment coefficient (Knoll, 2010). Because air is not one of these, every effort should be made to avoid air entering the counter and contaminate the gas. The electron attachment coefficient of oxygen in the air is relatively high, and will therefore form negative ions at a high rate. However, proportional counter need free electrons to multiply via ionization, as opposed to more

massive and thus slower ions. There is no gain for the ions because they have a low change in velocity, even in a strong electric field, because they are so massive. If oxygen is present, electrons heading towards the anodes will combine with the electronegative gas. If this happens, a negative ion goes to the anode rather than a free electron and the ion will fail to produce an avalanche. The result is that the pulse is small relative to those produced in pure gas and the pulse height spectrum has poorer resolution. There are two options; the gas can be permanently sealed within the counter or circulated through the chamber volume by a properly designed gas flow system. The first option of a sealed counter is the most practical because of the complications and physical restrictions involved with a continuous gas flow system. The only complications with sealed counters is they require extensive outgassing of materials including the TE plastic and their lifetime is sometimes limited by microscopic leaks that lead to gradual contamination of the fill gas.

The proposal in this research is to fill the detector at atmospheric pressure. Filling the gas at a much higher pressure will decrease the microscopic leaks in the detector and increase the lifetime of the detector.

2.5 Discussion of Uncertainties

Any measurement based on observing the radiation emitted in nuclear decay is a random process. There will be some degree of statistical fluctuations in any radioactive decay process. These fluctuations represent a source of uncertainty in all nuclear measurements that have to be accounted for. This applied when taking measurements

using an AmBe source but keep in mind that while radiation in space is not a nuclear decay process, it is a random process as well. The electronics and any other related measuring equipment can induced some uncertainties as well. Such as the setting of the amplifier gain for calibration. Uncertainties may also be introduced when filling the detector with the correct gas pressure and during the calibration procedure. The stochastic nature of energy deposition events by charged particles in the cavity of the detector, introduces some uncertainty. Another source of error is introduced when working with the raw data to calculate the microdosimetric quantities and the gain.

The size of errors depends also on the diameter of the detector. The smaller the diameter of the detector, the longer the measurement will be to get the desired number of counts. Since, for a Poisson random variable, the standard deviation is the square root of the number, the higher the counts, the higher the standard deviation is. When counting radiation(s) from a sample, the result is:

$$\text{counts} = n \pm \sigma = n \pm \sqrt{n} \tag{2.8}$$

Where n is the number of counts and $\sigma = \sqrt{n}$ represents one standard deviation based on Poisson statistics. Since the sample is counted for a specified period of time, the results are reported in units of time. Then the equation becomes:

$$\text{Count Rate} = R \pm \sqrt{R/T} \tag{2.9}$$

Where T is the sample counting time and R = n/T or counts per minute (cpm), counts per seconds (cps), etc.

Uncertainties for the average lineal energy distributions and the quality factor can be obtained by using the error propagation formulas (Knoll, 2010):

$$\sigma(\bar{y}_F) = \sqrt{\frac{1}{\sum_{i=1}^{N} f(y)} + \frac{1}{\sum_{i=1}^{N} d(y)}} \tag{2.10}$$

$$\sigma(\bar{y}_D) = \sqrt{\frac{\sum_{i=1}^{N} y^2\, d(y)}{\left[\sum_{i=1}^{N} y_i\, d(y)\right]^2} + \frac{1}{\sum_{i=1}^{N} d(y)}} \tag{2.11}$$

$$\sigma(Q) = \sqrt{\frac{\sum_{i=1}^{N} Q(y)^2 d(y)}{\left[\sum_{i=1}^{N} Q(y) d(y)\right]^2} + \frac{1}{\sum_{i=1}^{N} d(y)}} \tag{2.12}$$

CHAPTER III

DETECTOR DESCRIPTION

3.1 Assembly

The two detectors used for this study are a prototype dosimeter for the next generation of spacecraft and the International Space Station. The large detector, a 3.8 cm diameter, was designed and built at Texas A&M Nuclear Science Center (Perez-Nunez & Braby, 2011). The cathode (wall) is divided into 11 rings with 5 % voltage increments. The potential difference is adjusted between each ring and the anode to produce an electric field that is nearly constant along the length of the anode. This approach produces considerably less microphonic noise than detectors which use a helical grid (Braby et al., 1995). The cathode is made of tissue-equivalent plastic A-150. The wall thickness is 0.5 cm and was selected to provide sufficient buildup of delta rays into the spherical gas cavity and maintain charge particle equilibrium in the wall. The spherical shape was chosen for isotropic response.

The detector is covered by a gas tight chamber filled with propane at atmospheric pressure to simulate 68 µm site size. The charge sensitive preamplifier is inside the chamber to reduce electrical noise. The outer shield and chamber are made of aluminum and their wall thickness are 0.05 cm. The chamber‘s base is made of stainless steel which includes a bayonet system to compress an indium wire seal that reduces the total detector weight to less than half that of previous detectors of similar size (Perez-Nunez & Braby, 2011). Figure 3.1 shows the whole assembly of the 3.8 cm TEPC sphere

detector with the stainless steel base, aluminum chamber, aluminum outer shield, stainless steel bayonet, preamplifier and insulator.

Figure 3.1 Description of TEPC whole assembly (3.8 cm). From left to right: outer shield, chamber, detector, preamplifier, base, bayonet, and insulator. Reprinted with permission from Perez & Braby, 2011.

The TE A-150 plastic, manufactured by Exradin, is also known as Shonka tissue equivalent plastic. The A-150 is composed of 35.23% nylon, 45.12% polyethylene, 16.06% carbon, and 3.59% calcium fluoride by weight. Nylon is known to have hygroscopic properties. The hygroscopic properties of A-150 may cause the material to absorb minute amounts of water under certain conditions. This water can alter the physical characteristics of the material to an extent which may cause the ion chamber's measurements and calibration to change over time.

One of the many purposes of this study is to maintain the purity of the gas over long periods of time without the support of a gas purification system. In low earth orbit missions, a usable life of three years between gas changes is required (Braby et al.,

1995). For deep space missions a much longer useful life is required. One of the ways to maintain the purity of the gas and minimized leaking is by sealing the detector in a metal vacuum chamber. A vacuum chamber made of high z material will shield the detector from low energy photons and will scatter incident neutrons. On the other hand a vacuum chamber made of tissue-equivalent material has the effect of adding to the minimum depth in tissue at which the measurements of lineal energy can be made. The vacuum chamber used here is made of aluminum. The good electrical conductivity of aluminum means that it also shields the detector electrostatically to minimize the electronic noise.

The shape of the detector has a primary effect on the electrical and mechanical design. As discussed previously, the main advantage of a spherical detector is its isotropic response. Spherical detectors requires some mechanical modifications from the cylindrical detectors. Cylindrical detectors are easier to connect to a preamplifier and mount inside a vacuum chamber because of its shape, but for spherical detectors some extension has to be made at the end of the anode wire to provide a way of mounting the detector to the preamplifier. This modification could result in some wall thickness variations near the mounting region (Braby et al., 1995).

Once the detector has been assembled in the vacuum chamber and the aluminum outer shield, it is connected with a cylindrical aluminum mounting base as shown in figure 3.2. The cylindrical mounting base contains the circuits that connect the preamplifier to the shaping amplifier and the high voltage supply. The next step after the assembly is the leak testing and degassing and filling to the desired pressure with

propane gas on a gas filling system. This steps will be explain in details in chapter 4. The final step before testing the detector is to seal it off and disconnect it from the gas filling system. A cooper tube vacuum connection was sealed by the pinch-off technique which produces a cold weld at the end of the cooper tube. Sealing tubes with the pinch-off device produces ends which are clean and thin. The crimp-sealed tube must be handling with care to avoid disrupting the seal.

Figure 3.2 Cylindrical aluminum mounting base connected to detector

The selection of materials that can be used for insulators in the detector depends on the specific application and there are many different materials available for a single detector. The insulator used for this detector is Acetal plastic, most commonly known by the brand name Delrin (ePlastics, 1998). Delrin is a thermoplastic polymer

manufactured by the polymerization of formaldehyde. The chemical composition of acetal resins give parts made of acetal a combination of physical properties not available with metals or other plastics (ePlastics, 1998). The most important characteristic for this insulator in supporting the vacuum chamber may be outgassing rate and its mechanical strength. Acetal is known by its high strength, hardness, and rigidity under extreme temperature and humidity conditions.

The small detector, a 1.8 cm diameter, has not been used in space but is designed for long term space missions. The spherical shell has an inside diameter of 1.8 cm and an outside diameter of 2.4 cm. The wall material is also A-150 TE plastic. The wall thickness is 0.3 cm and was selected to provide sufficient buildup of delta rays into the spherical gas cavity without causing excessive fragmentation of high energy particles penetrating the wall or attenuation of MeV-energy neutrons (Straume et al., 2015). Unlike the 3.8 cm detector, the cathode for the 1.8 cm use field/shaping electrodes to reduce the electric field at the end of the anode. By reducing the electric field at the end of the anode, the electric field is constant along the anode wire and thereby the gain is constant through the gas volume. The 1.8 cm detector assembly is shown in figure 3.3. The detector is mounted on prototype boards with the anode insulators and a wire cage providing mechanical support at the top of the cathode. This type of assembly also helps to minimize noise caused by cathode vibration problems. The vacuum chamber is 0.01 cm thick aluminum with nickel-gold alloy plating on both the interior and exterior to provide good electrical contact to the base and provide electromagnetic shielding. To

seal the detector, the vacuum chamber and base plate are joined with screws compressing an indium wire gasket.

Figure 3.3 TEPC 1.8 cm detector assembly (left) attached to preamplifier circuit board enclosed in gold-plated vacuum chamber (right).

3.2 Electronics

TEPCs are operated in the pulse mode to record each individual energy deposition event. The charge collected in the detector is converted to a voltage pulse by the preamplifier. The output pulses are usually in the millivolt range. The charge Q is proportional to the energy deposited and is delivered as a transient current, where Q is the time integral of the current pulse (Knoll, 2010). A charge sensitive preamplifier with 1.04 pF feedback capacitor is used to convert the detector output to a voltage step and a

shaping amplifier is used to convert the voltage step to a nearly Gaussian pulse to reduce band width and therefore electronic noise. To process the pulses generated from the preamplifier, a pulse height analysis is required. For this study, a digital processing system was employed. The schematic diagram of this system is shown in figure 3.4. Pulses from the pre-amplifier are fed in parallel to two shaping amplifiers (Amplifier) with twenty times difference gain between them. The shaping amplifier is characterized by a shaping time constant that is closely related to the duration of the pulse produced at its output (Knoll, 2010). Pulse shaping helps minimize pile-up and overload and therefore maximize performance at high counting rates. This amplified signal is sent to the multichannel analyzer (MCA) to measure the pulse height for each event. MCA applies real time digital processing to the signal, increments a counter for the appropriate channel, and bins this value in its histogram memory generating an energy spectrum.

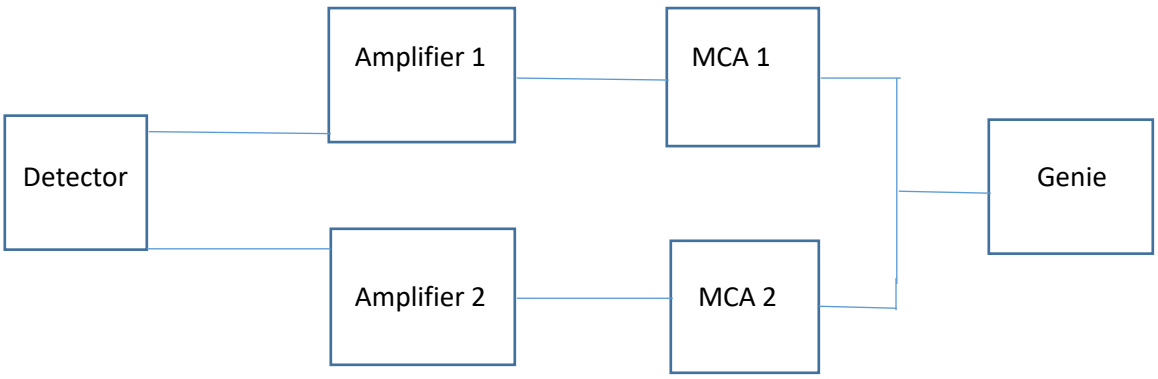

Figure 3.4 Schematic diagram of the detector and electronics.

The main purpose of pulse processing is to measure the detector signal with no distortion and to minimize electronic noise. The charge sensitive preamplifier used in this study convert the charge pulse produced by an energy deposition event to a voltage peak. The block diagram of a simple charge sensitive preamplifier is shown in figure 3.5. The charge from the detector is deposited at the negative input of the operational amplifier. The output voltage goes to the feedback capacitor, C1, which collects the charge from the detector. The output voltage also increases until the potential difference between the plus (+) and minus (-) inputs is zero (Straume et al., 2015). R1 is used to decrease the charge of C1 to prevent output voltage from reaching the amplifier's maximum voltage when more charge is received from the detector.

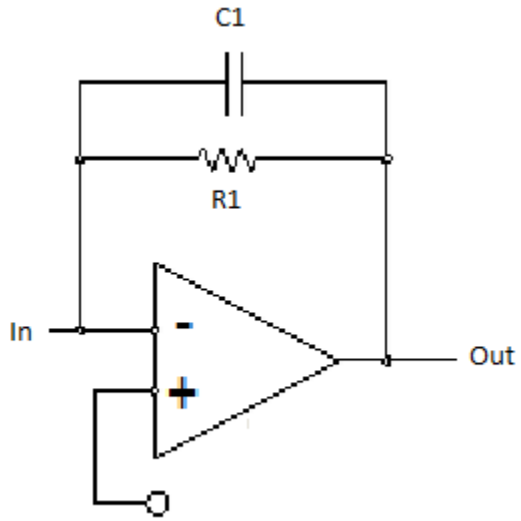

Figure 3.5 Block diagram of a charge-sensitive preamplifier circuit.

The charge sensitive preamplifier has proven to be an extremely useful low-noise circuit. Placing the preamplifier inside the vacuum chamber eliminates the capacitance to ground that otherwise takes place when the preamplifier is outside the vacuum and thus reduces the electronic noise.

The shaping amplifier output signal is the input to the MCA where the analog signal is converted to an equivalent digital number. The analog-to-digital converter (ADC) constitutes an important element in determining the performance characteristics of the analyzer. The ADC derive a digital number that is proportional to the amplitude of the pulse presented at its input. In this system, shown in figure 3.6 and 3.7, the MCA detects the amplitude of the peak of the shaped pulse, using a digital peak detect circuit, and assigns a channel number. The voltage that corresponds to these channels are zero to ten volts.

Figure 3.6 The signal processing system: Amplifier, high voltage supply, and MCA.

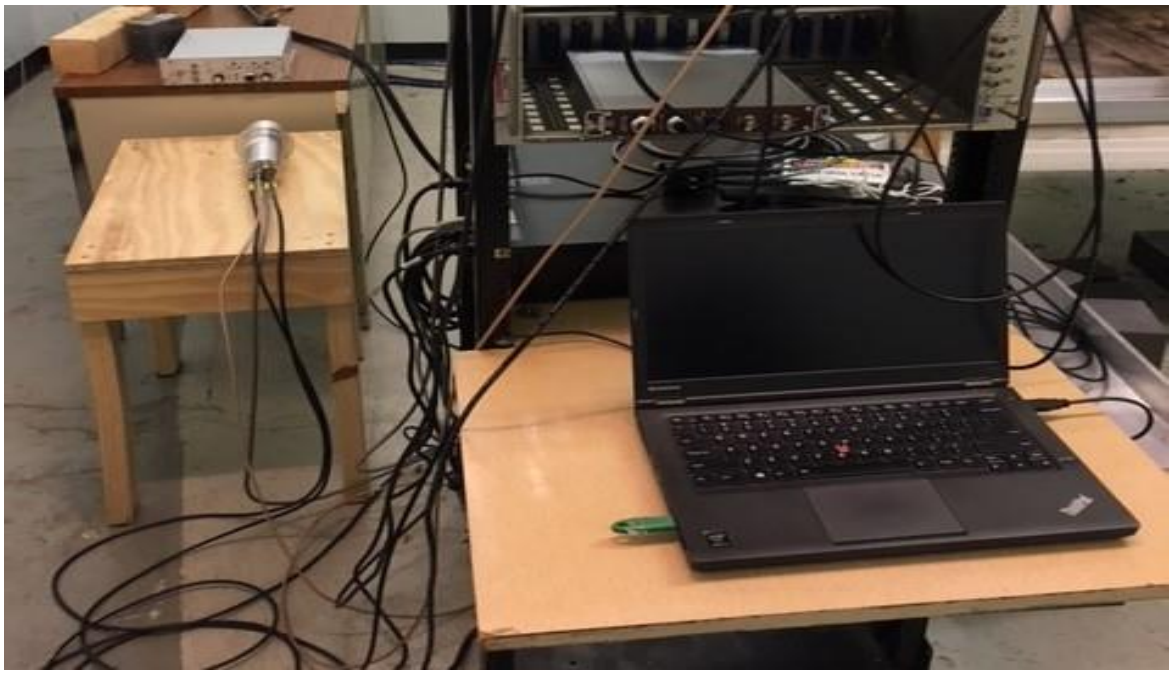

Figure 3.7 The 3.8 cm detector connected to the signal processing system and computer.

Data is transferred to the computer via USB in approximately real computer time. The GENIE 2000 software provides the access to all the required configurations parameters includes simple analysis, spectrum, and the ability to save the data in suitable format.

3.3 MCNP6 Simulation

The MCNP6 is a general purpose, continuous-energy, generalized-geometry, time-dependent, Monte Carlo radiation transport code designed to track many particles types over broad ranges of energies. It can be used for neutron, photon, electron, charge particle or coupled neutron/photon/electron transport (Los Alamos National laboratory, 2017). The code treats an arbitrary three dimensional configuration of material in geometric cells bounded by first and second degree surfaces and fourth degree elliptical tori. The MCNP original code was developed around 1957 by Los Alamos National laboratory. Several improvements have been made throughout the years with different upgrade versions. The current version MCNP6 used in this study is described as the merger of MCNP5 and MCNPX capabilities, which is the result of five years of effort by the MCNP5 and MCNPX code development teams.

The MCNP6 code has been expanded to handle a multitude of particles and to include model physics options for energies above the cross section tables and for delayed particle production (Oak Ridge National Laboratory, 2014). For neutrons, all reactions given in a particular cross-section evaluation are accounted for. Thermal neutrons are given as both the free gas and alpha/beta models. For photons, the code accounts for

elastic and inelastic scattering, absorption (pair production/annihilation), and bremsstrahlung

This MCNP6 Monte Carlo code was used to simulate the behavior of both detectors using an AmBe neutron source. The simulation was done to replicate the experiments and the results from the simulations will be compare with the experimental results from the lab in section 4.3.2 and 4.3.3. The program was set up to calculate the neutron flux, the dose rate, and f(y) in a spherical detector (3.8 cm & 1.8 cm) at 8 cm from the source. The spherical detector is filled with propane with a density corresponding to the pressure to simulate a site size of 68 μm and 32 μm for the large and small detector respectively as well as 2 μm for both detectors in table 3.1. The AmBe neutron source is a point isotropic source located 8 cm away from the center of the 3.8 cm detector and 15 cm away from the center of the 1.8 cm detector. It emits 6.4 x 10^6 neutrons per second of average energy 4.5 MeV.

Table 3.1 Large and small detector density and pressure of propane gas

Site Size	Pressure (torr)	Density of gas	Detector
32 μm	760	1.8×10^{-3} g/cm^3	1.8 cm
68 μm	760	1.8×10^{-3} g/cm^3	3.8 cm

The simulations were run using the same conditions as the experiment set up. The detector was simulated as a tissue equivalent plastic spherical shell, filled with propane surrounded by an aluminum vacuum chamber and an outside aluminum shell. The material composition for A-150 plastic is shown in table 3.2.

Table 3.2 Elemental composition of A-150 tissue-equivalent plastic. Reprinted with permission from American Association of Physicist in Medicine, 1980.

Element	Percent by weight
H	10.2
C	76.8
N	3.6
O	5.9
F	1.7
Ca	1.8

The A-150 tissue-equivalent plastic simulates muscle tissues due to similar compositions.

The geometry has 8 cells and 10 surfaces. Cell 1 is the AmBe source cylinder, which is located 8 cm away from the 3.8 cm detector and 15 cm away from the 1.8 cm detector. Cell 2 is the outer shield aluminum wall and cell 3 is the space between the outer shield and the chamber. Cell 4 is the chamber aluminum wall and cell 5 is the

space between the chamber and the detector wall. Cell 6 is the detector spherical wall. Cell 7 is the inside of the sphere and cell 8 is the void between the source and the detector.

Cell cards are used to enter the material composition and density. The material is described on a material card (m) that has the same material number. This specification includes a list of the signed surfaces bounding the cell where the sign denotes the sense of the regions defined by the surfaces. The regions are combined with the Boolean intersection and union operators where a space indicates an intersection and a colon indicates a union (Oak Ridge National Laboratory, 2014).

Surface cards are used to indicate the surface type and dimensions of the surfaces. SO is for sphere and C/Z is for a cylinder. This simulation used the AmBe neutron source as a cylinder and the detector as a sphere.

The Mode card consist of the mnemonic mode followed by a list of particles to be transported. If the mode card is omitted, mode n is assumed (neutron transport only). For this simulation, neutrons and protons were considered, so the code "mode n,h" was used.

The Data cards consists of source specification (SDEF), tally specification (F4, F8), average flux to dose rate conversion factors (DE, DF) and material specification (m). The neutron flux was estimated using the tally F4 (cm^{-2}), which calculates the average flux over a cell (particles/cm^2). The absorbed neutron dose rate was obtained through tally F14 (R/hr.), which considers the neutron energy deposition average over the cell. This tally gives the energy deposited per unit mass of the material. The

conversion from R/hr to Gy/hr is obtained by multiplying the R/hr value by 8.7×10^{-3} since $1R = 8.7 \times 10^{-3}$ Gy. The pulse height distribution was obtained using the F8 tally to get the number of events per deposited energy interval. The importance of the overall geometry were selected as equal (=1), excluding the space between the sphere and source. The f(y) or d(y) of the experimental and simulated results are compared in chapter 4. Comparison of simulated and measured absorbed dose has large uncertainty because of uncertainty in neutron flux from source, therefore is better to compare the f(y) and d(y) distributions.

Finally, GCR particle simulations were performed modeling the detector response in MCNP using the F8 tally. These simulations are useful to show the difference in results for 2 μm, 32 μm, and 68 μm simulated site sizes. This is needed to determine if 32 μm and 68 μm sites can give good measures for radiation quality in space. The F8 tally is the pulse height tally. The pulse height tally is analogous to a response from a physical detector and provides the energy distribution of pulses created in the designated cell. The designated cell is the same as for the 3.8 cm detector with the exception of the outer shield and chamber which was not included for this simulations because it would not make much difference for space radiation particles. The cell tally was modified using an energy card dividing the pulse height into energy bins corresponding to the total energy deposited in a detector by each physical particle history. The model only accounted for the small sphere and a bigger sphere that surrounds it. This bigger sphere is where the GCR particles are generated and the small

sphere is the detector. A sample input deck for the simulation is shown in the Appendix and the results are shown in chapter 4.

The GCR particles considered for this model were protons, alpha particles (helium), and iron ions distributed to generate a uniform and isotropic flux inside the sphere. The heavy ions that can be transported in Monte Carlo is any ion heavier than helium ($z > 2$) and it was chosen iron ion as initial source particle using PAR=26056. The SUR card is used for a distribution on a surface. In this case SUR=1 is the surface source that surrounds the cell of interest. NORM= -1 emitted all particles inward on surface 1 in a cosine distribution towards the cell of interest. In space radiation, GCR particles can generate energies primarily between 10 MeV/n up to over 20 GeV/n. The main purpose of this simulation is to determine if 32 μm and 68 μm site sizes can give good measures for radiation quality in space, it is not to calculate the dose rate or equivalent dose. Thus the main focus was to provide models with energies high enough to represent the GCR energies in free space disregarding the exact distribution or flux of the particles. The GCR energy range considered was from 10 MeV/n to 20 GeV/n. No shielding was present for the first calculation. For the second calculation the Badhwar-O'Neill spectrum was used which is a distribution of GCRs distribution of energies from 0.001 MeV/n to 20 GeV/n behind 20 g/cm^2 aluminum shielding.

The y distributions were obtained using the F8 tally and E8 energy functions. In this manner the output is similar to the output of a multi-channel analyzer. The data was transferred to excel to histogram the data and calculate $\bar{y}_F$ and $\bar{y}_D$. In addition, the histogram program in excel calculated the average quality factor.

CHAPTER IV

RESULTS AND DISCUSSION

4.1 Detector Calibration

4.1.1 Determination of Proton Drop Point

Calibration and measurements were taken at Texas A&M Nuclear Science Center. Prior to the measurements, the detectors were filled with pure propane gas at a pressure according to the corresponding site size. Pure propane gas was chosen due to its better gain properties than methane based tissue equivalent gas. For the low pressure, it will be the pressure corresponding to the 2 µm size, and for the atmospheric pressure, the pressure will be 760 torr which corresponds to a site size of 68 µm for the 3.8 cm detector and 32 µm for the 1.8 cm detector. Site size can be changed by changing gas pressure as shown in table 4.1 for the two detectors in this study. The pressure can be obtained by using the ideal gas constant relationship:

$$P.V = n.R.T \tag{4.1}$$

Where R = 8.31 x 10^3 cm^3 KPa / mol.K and T = 298.15 K. We can rewrite equation 4.1 in terms of density to get the gas pressure required to simulate different site sizes:

$$P = (\rho.R.T) / M \tag{4.2}$$

Where M = 44.096 g/mole, molecular weight of pure propane gas and ρ is the density of the gas. The density of the gas, which controls the site size simulation, can be obtained from:

$$\rho_g.d_g = \rho_t.d_t \qquad (4.3)$$

where ρ_g is the density of the gas, d_g is the diameter of the gas cavity, ρ_t is the density of the tissue, and d_t is the simulated site size diameter. For a 3.8 cm detector simulating a 2 μm site size, we get d_g = 3.8 cm, $d_t = 2 \times 10^{-4}$ cm (2 μm), and ρ_t = 1.0 g/cm^3.

The procedure for filling the gas is to initially pump down to 1×10^{-3} torr by using a rotary pump. The detector is then filled with counter gas to about 760 torr and pumped down to 1×10^{-3} torr. This procedure is to be repeated at least three times. The detector is next filled to the proper pressure for operation. Once the detector is filled with propane gas and sealed, then it is ready for calibration. At the lab the detector was placed 8 cm from the AmBe source and the spectra was acquired for 21600 seconds (6 hrs.). The 6 hours was sufficient time to get enough counts to resolve the proton drop point. The AmBe source has a half-life of 432 years and activity of 2.36 Ci which is approximately 6.4×10^6 n/s.

Table 4.1 Gas pressure and density of the counting gas.

Site Size	Pressure (torr)	Density of gas	Detector
2 µm	47	1.1×10^{-4} g/cm^3	1.8 cm
32 µm	760	1.8×10^{-3} g/cm^3	1.8 cm
2 µm	22	5.3×10^{-5} g/cm^3	3.8 cm
68 µm	760	1.8×10^{-3} g/cm^3	3.8 cm

The calibration of the detector is the determination of a calibration factor which is the quotient of the lineal energy and the proton drop point obtained under well-defined measuring conditions:

$$CF = y / PDP \tag{4.4}$$

Where CF is the calibration factor, y is the lineal energy as defined in equation 1.4, for the proton drop point and PDP is the MCA channel number of the proton drop point. The proton drop point is the maximum energy deposited by a proton at the end of the range. The CF is used for the conversion of the MCA channels into lineal energy, the "y" value calculated from energy loss of the secondary particles divided by the mean chord length. For example, the lineal energy of the proton drop point for a detector simulating a 2 µm site size is the energy imparted divided by the mean chord length. The energy imparted ε is the site size multiplied by the maximum proton linear energy transfer (LET) in tissue averaged over a distance equal to the detector diameter:

$$\varepsilon = 2\ \mu m \times 100\ keV/\mu m = 200\ keV \quad (4.5)$$

and the mean chord length for a sphere detector is:

$$\bar{l} = (2/3)^* d \quad (4.6)$$

Where d is the site size. In this case d = 2 µm, so we get $\bar{l}$ = 1.33 µm. Then y = 150 keV/µm. If the proton drop point is channel 215, then the CF = 150 keV/215 = 0.7 keV μm^{-1} $channel^{-1}$. This number is multiplied by the channel number to get the calibrated lineal energy for measurements with this detector. Since TEPC are not absolute devices they have to be calibrated in terms of event size. The main goal of the calibration is to convert the pulse height corresponding to the energy loss of a secondary particle crossing the cavity into energy imparted or the related lineal energy y. The maximum proton LET for a 2 µm site size was determined to be 100 keV/µm. The LET for a 32 µm and 68 µm site size was obtained using the NIST range data. The NIST range data was accessed at https://www.nist.gov/pml/stopping-power-range-tables-electrons-protons-and-helium-ions online. It is a database that calculates stopping-power and range tables for electrons, protons, or helium ions in according to methods described in ICRU report 37 and 49 (Berger et al., 2017). For this research the proton tables is used to get ε. The material considered was A-150 tissue equivalent plastic or you can also use water (liquid) and the range was continuous-slowing down approximation (CSDA) range. For the 68 µm case, the CSDA range was 6.8 x 10^{-3} cm and using the tables and

tabulating we get ε = 1875 KeV. Following the same procedure for the 32 μm case, the CSDA range was 3.2 x 10^{-3} cm and the energy imparted ε = 1200 keV. To get average LET, the energy imparted ε is divided by the site size. Then the maximum average proton LET for the 32 μm and 68 μm is 37.5 keV/μm and 27.5 keV/um respectively.

The detector was exposed to an AmBe source and using the shaping amplifiers and MCA the pulse height spectrum was collected. The proton drop point was obtained by a visual inspection of the spectrum where the sharpest drop in the spectrum is observed.

4.1.2 Gas Gain

In proportional counters a number of primary electrons not attached by electronegative molecules (i.e oxygen) will reach the anode wire where they are amplified up to 10^3 or 10^4 times by the high voltage applied to the anode. This is known as gas multiplication and is a consequence of increasing the electric field within the gas to a sufficiently high value (Knoll, 2010). Thus because of gas multiplication process a single electron can produce an electron avalanche. The formation of an avalanche involves many interactions with atoms in which a variety of excited atomic or molecular states may be formed (Knoll, 2010). When electrons are released in the sensitive volume of gas-filled detectors, primary electrons undergo well known elastic and inelastic processes.

The gas gain for each of the primary ionizations can be defined as the average number of electrons collected at the anode. In section 2.3 gas gain was described as a

general analysis of proportional counters operations based on the assumption of exponential growth of the electron avalanche. The experimental gas gain was obtained by studying the detector response to an AmBe source. The detector output was connected to a charge sensitive pre-amplifier, described earlier in section 3.2, with a measured test capacitance of 1.04 pF (The same as the feedback capacitance). The output from the pre-amplifier was fed to two shaping amplifiers to cover the wide range of energy deposited. Shaped pulses were converted by an MCA to digital numbers which provide pulse height processing over the large dynamic range. Calibration of microdosimetric spectra in terms of lineal energy y was performed using the proton drop point (PDP). The gas gain "G" of a proportional counter is defined as the ratio N/ N_o where N_o is the number of electrons at the output of the detector and N is the initial number of electrons produced in the sensitive volume by the incident radiation (Moro et al., 2014).

The measured proton lineal energy distributions are used to calculate the gain in the following manner. The lineal energy of the proton edge is used to calculate the number N of the initial electrons produced in the gas volume of the detector. A voltage pulse is fed into the test input of the amplifier to reproduce the output signal of the electron edge. The channel number, h_c, of this pulse is used to calculate the final number N_{out} of electrons after the gas amplification (Moro et al., 2014). To calculate G, the following equation is used:

$$G = \{(V_T.C_{test} / e.h_c)*PDP\} / \{(y.\bar{l}) / \omega\} \quad (4.7)$$

Where the first bracket is the N_{out} and the second is the N_{in}. V_T is the test pulse voltage amplitude in terms of millivolts, C_{test} is the capacitance, e is the electron charge, and h_c is the channel number at the test pulse. The $\bar{l}$ is the mean chord length and will cancel when multiply by y because $y = \varepsilon / \bar{l}$ and we will get ε, the energy deposited in the cavity. The average energy per ion pair ω is the energy needed to form one ion pair. This energy depends on the counter gas used. ICRU report 31 recommended value for propane is ω = 26.2 eV/pair (ICRU, 1979). The gas gain G is then defined as:

$$G = \{(V_T.C_{test} / e.h_c)*PDP\} / \{\varepsilon / \omega\} \quad (4.8)$$

For the 3.8 cm detector simulating a site size of 2 μm, V_T = 80 mV, the channel number h_c = 30, the PDP is 215 and the energy imparted is ε = 200 keV. The input capacitance C_{test} = 1.04 pF and ω = 26.2 eV/pair and plugging these numbers into equation 1.25 we get a gas gain of 469. For this research the gas gain will be calculated as a function of voltage from 600 V to 800 V in increments of 50 V.

4.2 Microdosimetric Quantities

In the application of experimental microdosimetry it is possible to determine the portion of absorbed dose contributed by neutrons only. The determination of neutron dose equivalent has always been quite difficult. The definition of dose equivalent, as the product of absorbed dose and the quality factor, was a simple concept that was difficult to apply in practice. The quality factor is defined as a function of linear energy transfer

(LET), but the LET distribution generated by a particular radiation has proven to be nearly impossible to measure. Rossi developed a new quantity, lineal energy that was related to LET and could be measured using the TEPC. For this research the average quality factor Q can be calculated as:

$$Q = \sum_{i=0}^{\infty} Q(y_i).\, y_i.\, N_i / \sum_{i=0}^{\infty} y_i.\, N_i \qquad (4.9)$$

Where N is number of events, y_i is channel number times the calibration factor, and Q, according to ICRP 60, is defined in terms of LET:

$Q = 1$	$L < 10$ keV/μm
$Q = 0.32L-2.2$	$10 < L < 100$ keV/μm
$Q = 300/L^{1/2}$	$L > 100$ keV/μm

For evaluation of dose equivalent in space it is common to assume that the lineal energy (y_i) of a charged particle that traverses the gas cavity is equal to this unrestricted LET. This is not completely true since the lineal energy of such particle will fluctuate about the actual unrestricted LET which is defined as the expectation value of energy loss at a point.

The total deposited energy (absorbed dose) in the gas cavity can be obtained by summing up the energy deposited by each individual event. The absorbed dose in a microdosimetry tissue volume D_t is the same as that simulated by a low pressure gas cavity of diameter d_g given by:

$$D_t = \varepsilon/m = \bar{l}. \sum_{i=0}^{\infty} y_i . N_i \, / \, m \quad (4.10)$$

Where $\bar{l}$ = mean chord length defined in equation 4.6 and $m = \rho_g.\pi/6.(d_d)^3$ for a spherical detector. This mass of the counter gas m depends on the geometry of the counter. The units for D_t in equation 4.10 are keV/kg, so we need to multiply by 1.602×10^{-16} J/keV to convert to Joules (J), where J/kg is equal to the absorbed dose unit Gray.

The frequency-mean lineal energy $\bar{y}_F$ and dose-mean lineal energy $\bar{y}_D$ will be calculated using the following equations:

$$\bar{y}_F = \sum_{i=0}^{N} y_i . f(y_i) \, / \, \sum_{i=0}^{N} f(y_i) \quad (4.11)$$

$$\bar{y}_D = \sum_{i=0}^{N} y_i^2 . f(y_i) \, / \, \sum_{i=0}^{N} y_i . f(y_i) \quad (4.12)$$

Results obtained when measured by detectors at atmospheric pressure will be compared with results obtained when measured by the detectors at low pressure and with MCNP6 results. These comparisons will help to determine if both detectors can accurately measure the equivalent dose and absorbed dose rate at atmospheric pressure.

4.2.1 Site size effects

One influence on the shape of the microdosimetric spectra is the simulated site size. An increase of simulated site size causes narrowing of the distribution because of reduction of straggling (Farahmand, 2004). As the site size increases, the spectra shift to lower lineal energy values. One way of explaining this is considering the initial proton

recoil flux in the cavity. For a 2 μm simulated site size, most of the recoil protons cross the cavity, producing a relatively sharp peak in microdosimetric spectrum. As the simulated site size increases above 2 μm, protons deposit an increasing fraction of their energy within the cavity. If the protons stop in the cavity, increasing the simulated site size does not increase the energy deposition, and therefore the whole spectrum is shifted toward lower y values. Therefore the proton drop point shift downward because at the very larger sizes the maximum energy that protons can expend in the cavity is less than the product of the maximum average LET and the diameter.

In order to understand the energy imparted, it is also useful to distinguish between five classes of particle tracks as shown in figure 4.1. The particle tracks depends on the location of their production with respect to the sensitive volume. The five classes of particle tracks are:

1. Insiders = Particles originating and stopping in the volume may lose their entire energy in the volume.
2. Starters = Particles originating in the volume may leave the volume before losing all their energy.
3. Stoppers = Particles originating outside the volume may enter the volume and stop within the volume.
4. Crossers = Particles originating outside the volume may cross the volume, depositing only part of their energy in the volume.
5. Touchers = Particles originating outside the volume may not enter the volume in a straight line but by straggling or their delta rays.

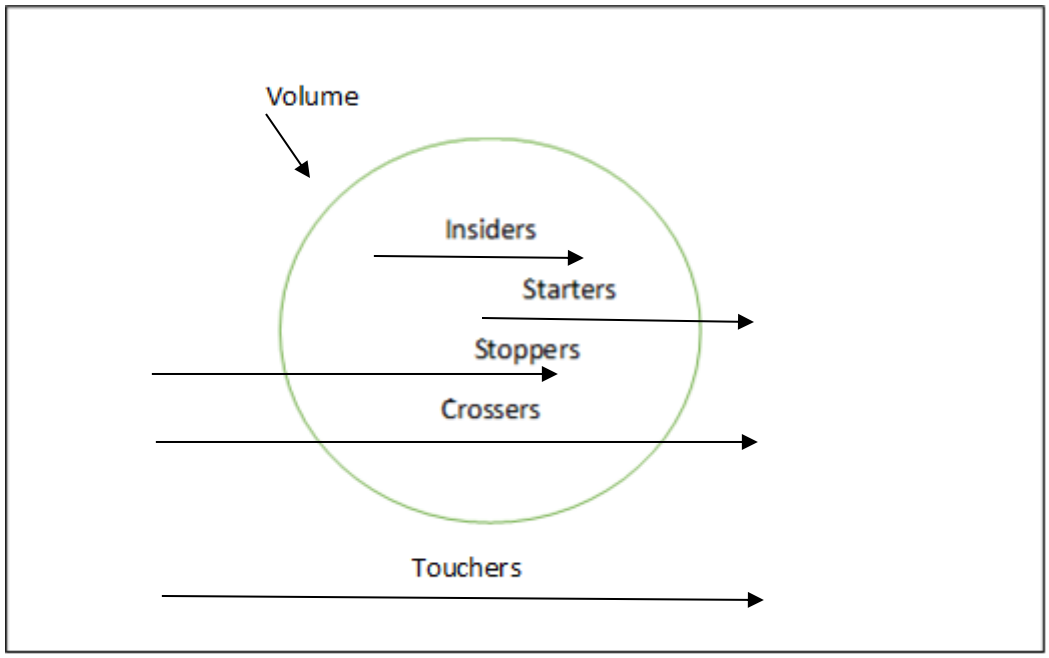

Figure 4.1 Classification of charged particle tracks with respect to their production to the sensitive volume.

In space radiation the largest contribution is coming from the crossers as expected since the range of the most particles is much larger than 2μm, 32 μm, and even 68 μm sensitive volume size. As the charged particles energy increases and the range of the particles increases, the contribution of insiders decreases while the contribution of crossers increases. The 68 μm proton peak should be higher than the 2 μm, and 32 μm peak because a larger fraction of the energy transferred to delta rays is deposited in the site.

4.3 TEPC's characteristics at low and atmospheric pressure

As was indicated in the first chapter, one of the main concerns when using TEPC in a long term space mission is the potential for vacuum leaks in the detector. To eliminate the potential for any leaking it was proposed to fill the detectors with pure propane gas at atmospheric pressure. This was done for both detectors used in this research. The detectors were tested and validated at the Texas A&M Nuclear Science Center. The testing was done by using an AmBe source with average neutron energy in the MeV region and the validation was done by comparing the measured microdosimetry spectra at atmospheric pressure and at low pressure with calculated spectra at the relevant site sizes. The relevant microdosimetry quantities include dose-mean lineal energy $\bar{y}_D$, frequency-mean lineal energy $\bar{y}_F$, and average quality factor.

For all the measurements taken a pulse height spectrum was recorded as described in section 3.2. The microdosimetric data analysis caries out a normalization of the frequency and dose distribution such that the area under the frequency and dose distribution curve presents a probability of 1.0. A more concise and complete information is obtained from the plot of yd(y) as a function of the log of lineal energy, y, where the area delimited by any two values of lineal energy y, is equal to the fraction of dose delivered in that interval.

4.3.1 Gas Gain for the 3.8 cm and 1.8 cm detector

Numerous studies have been done to derive a general expression describing the gas gain in TEPCs. The gas gain expression used here was defined in section 4.1.2. It is

generally based on the assumption of exponential growth of the electron avalanche. The gas gain G, is the ratio of the number of electrons, resulting from multiplication, and the initial number of electrons. The gas gain was taken at five different voltages: 600, 650, 700, 750, 800 volts to determine the detector optimal performance in terms of gas multiplication. These measurements were taken at simulated site sizes of 2 μm, 32 μm and 68 μm. The gas gain as a function of voltage is shown in figure 4.2 and 4.3. The departure from linearity starts taking place after a voltage of 750 V for both site sizes. Above 950 V the detector will reach a point beyond which there is significant departure from linearity. Below 400 V the voltage is high enough so that there is no recombination, but is not high enough to cause gas multiplication. For the 3.8 cm diameter detector we can see that for each 50 V increase there is a factor of 1.5 gas gain increase for the 2 μm site size. On the other hand, for the 68 μm site size the gas gain factor increase from 600 to 650 V is 1.9 but from 650 V to 800 V it goes back down to 1.5 per 50 volts. There is a similar situation for the 1.8 cm diameter detector where for each 50 V increase there is a factor between 1.5 and 1.6 gas gain increase for the 2 μm site size and 1.6 for the 32 μm site size.

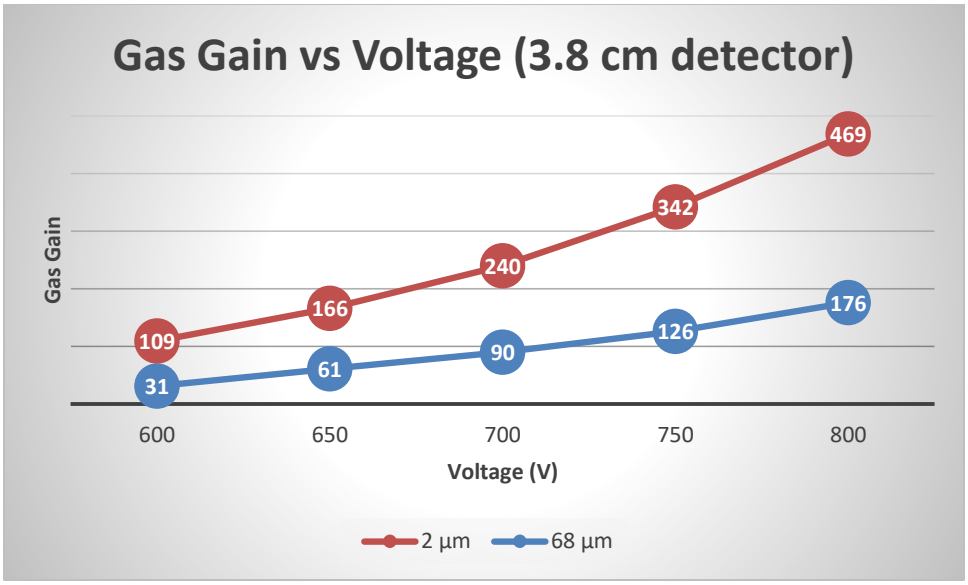

Figure 4.2 Gas Gain as a function of voltage for the 3.8 cm detector

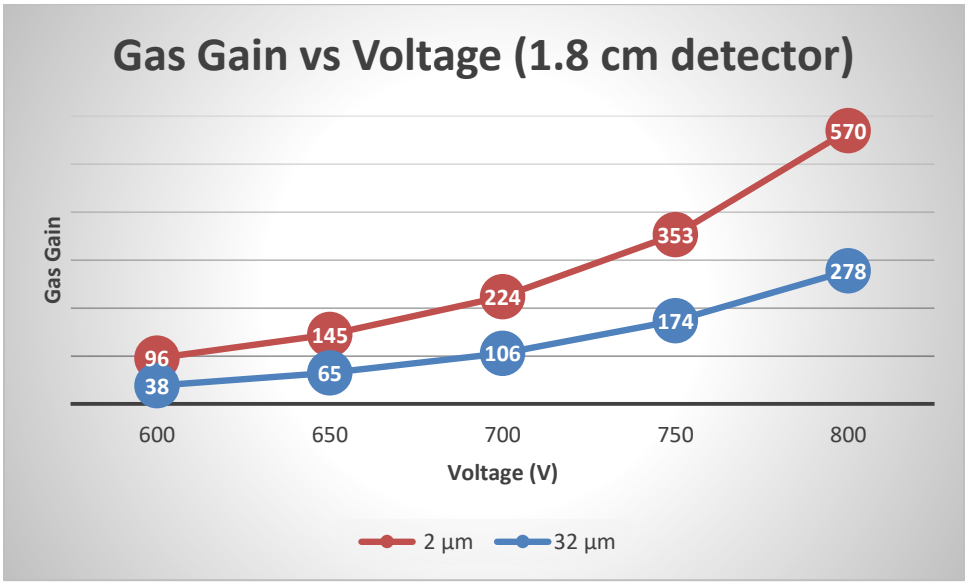

Figure 4.3 Gas Gain as a function of voltage for the 1.8 cm detector

The gas gain is higher at a lower counter gas pressure than at atmospheric pressure. This could be related to the electron mobility. When using a proportional

counter, gas multiplication occurs only in the immediate vicinity of the anode so the electrons liberated anywhere in the counter volume are equally multiplied. However, as the pressure of the counter gas is reduced the multiplication region extends to increasing radial distances resulting in a longer avalanche and increase in gain. Also, electrons in gas at lower pressures may circle the wire and undergo one or more further collisions before being absorbed in the wire, further increasing the gas gain at the same voltage. At lower pressures the energy imparted by a charged particle that crosses the site is less than at higher pressures. For example, at a low pressure simulating a site size of 2 μm, the energy imparted by a particle with dE/dx = 100 keV/μm, assuming dE/dx does not change, is 200 keV. At Atmospheric pressure simulating a site size of 68 μm, and the electronic noise level does not change, the energy imparted is 1870 keV. Since the energy imparted is much greater at atmospheric pressure, a lower gas gain will result in the same signal to noise level and allow detection of low LET events.

4.3.2 The 3.8 cm diameter detector

An assessment of the performance of both detectors has been done through measuring microdosimetric event-size spectra for neutrons produced by the AmBe source and by simulation of energy deposited by the AmBe neutrons using MCNP6 codes. The results with the neutron source and the MCNP6 simulations for the 3.8 cm detector are presented here and the results for the GCR simulations are presented in section 4.4. Results for the 1.8 cm detector are presented in section 4.3.3.

Figure 4.4 shows the microdosimetric event size spectra for the 2 µm site size. The general shape of the spectra is what would be expected for AmBe neutron energy spectrum. The peak found between 10 keV/µm and 100 keV/µm is the proton peak with a maximum around 39.1 keV/µm. This peak is the product of the interaction of recoil protons. At the high lineal energy side of the spectra is the "proton drop point" which is the point where the recoil proton deposit their maximum amount of energy possible around their maximum stopping power when interacting with the simulated volume.

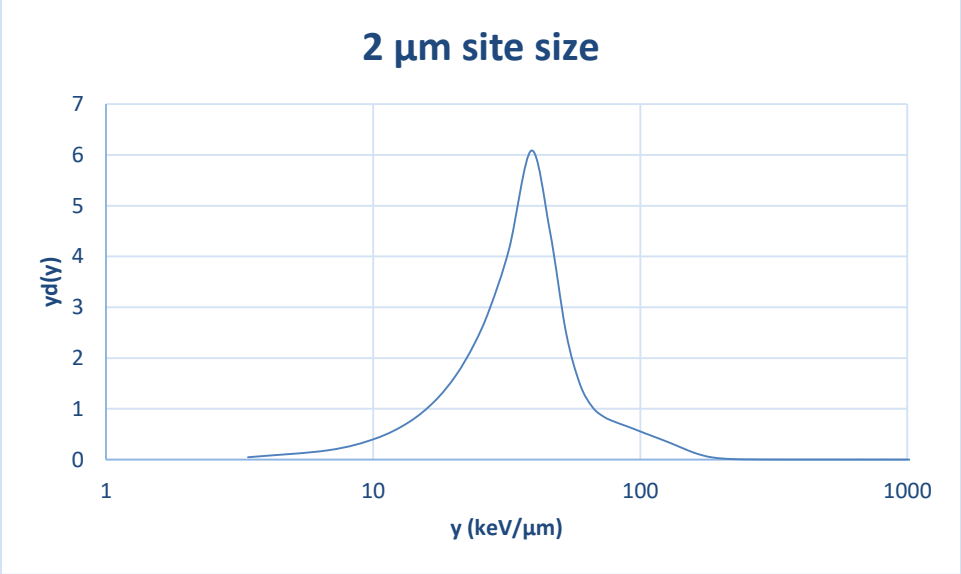

Figure 4.4 Lineal energy spectra for the 2 µm site size measured with the 3.8 cm detector.

The spectra obtained using MCNP6 codes simulation is shown in figure 4.5. The proton peak is found around 38.3 keV/µm which is very close to the 39.1 KeV/µm peak found in the experimental spectra. The small peaks between 1 keV/µm and 10 keV/µm which corresponds to ionizing electrons are more visible in this spectra than the

experimental spectra. This could be due to better resolution when using the Monte Carlo codes which make it easier to see those small events. The small peaks at the high energy tail belongs to alpha particles and heavy recoils above 2.25 MeV. These peaks are very small here but they become very significant and more noticeable at higher neutron energies. For the space radiation particle spectrum these high lineal energy peaks are the point of interest because of the influence of very high energy alpha particles and heavy ions.

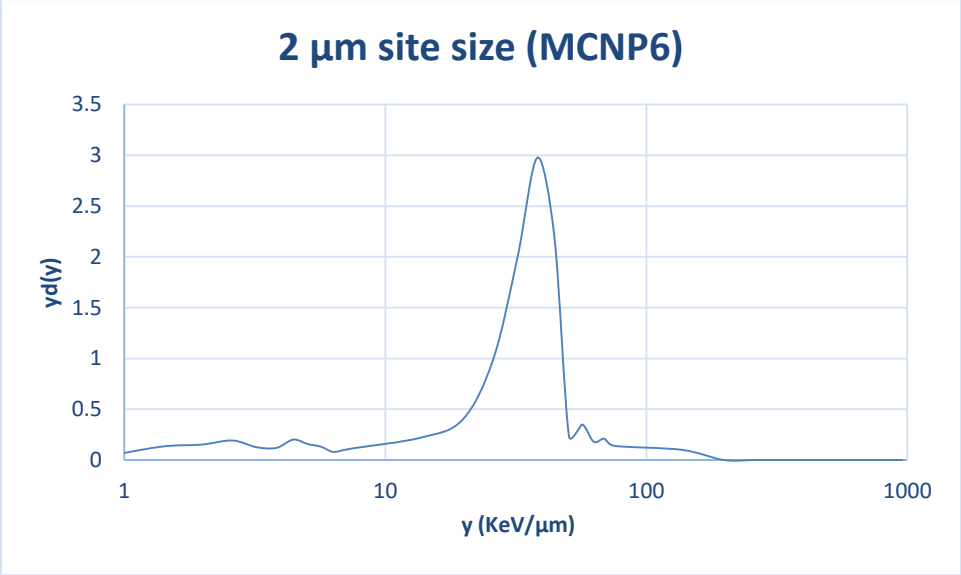

Figure 4.5 Lineal energy spectra for the 2 µm site size using the MCNP6 simulation.

The measured lineal energy spectra of the 68 µm site size is shown in figure 4.6. The proton peak maximum is around 32.3 keV/µm.

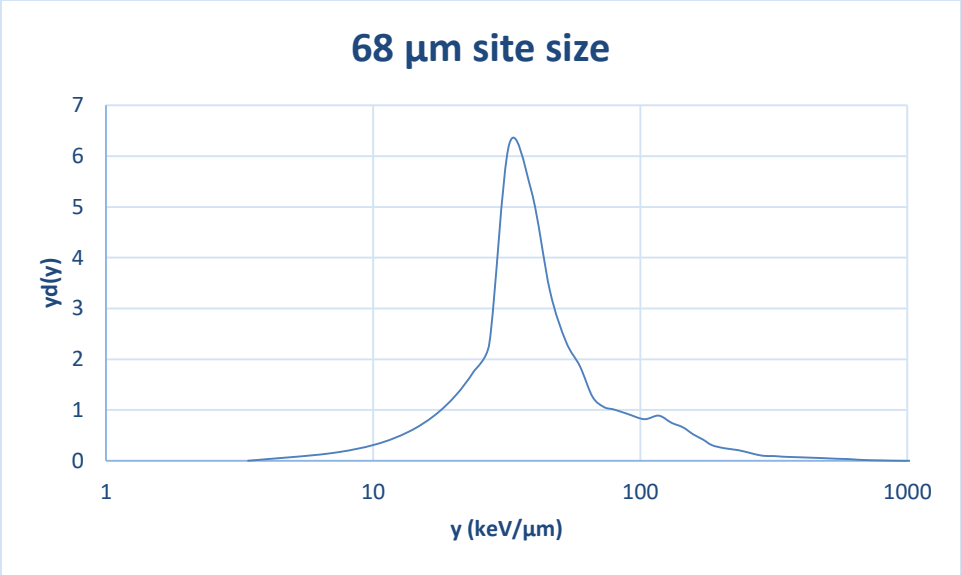

Figure 4.6 Lineal energy spectra for the 68 µm site size measured with the 3.8 cm detector.

The change in the shape of the spectra with simulated site size is shown in figure 4.7. The proton peak is higher for the 2 µm site size because there are very few protons that stop in this small distance. The protons generated inside the cavity and the walls of the counter have a range greater than the mean chord length of a 2 µm simulated size. Therefore, the width of the event size spectrum is determined by energy loss fluctuations of the protons due to changes in path-length and stopping power. The lineal energy "y" spectra shift to lower lineal energy values as site size increases. This is because as the site size increases, the energy imparted by insider and stopper secondary particles is divided by a larger mean chord length. The largest contribution of secondary particles is coming from crossers as expected since the range of the most secondary particles is much larger than the 2 µm and 68 µm site sizes. The percent of crossers is higher for the 2 µm site size.

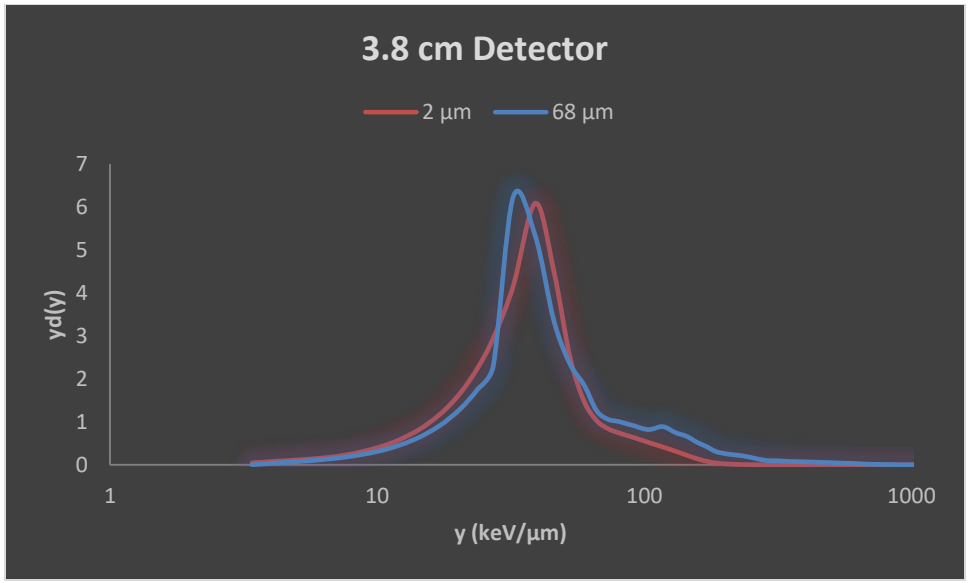

Figure 4.7 Lineal energy spectra for the two site sizes for the 3.8 cm Detector.

A comparison with the MCNP6 simulated spectra for the 68 µm site size confirm our experimental spectra results. The lineal energy spectra for this simulation is shown in figure 4.8. The proton peak maximum is round 31.0 keV/µm. The measured and calculated spectra compare well and the proton peak and proton drop point appear around the same location in the energy spectra. Here again we found a sharper proton drop point and a more defined proton peak as we would expect from a simulation. The difference in the spectra may be due to noise caused by the instruments and the variance in the gas gain not accounted for in MCNP6, in addition to uncertainties during the calibration and measurement process.

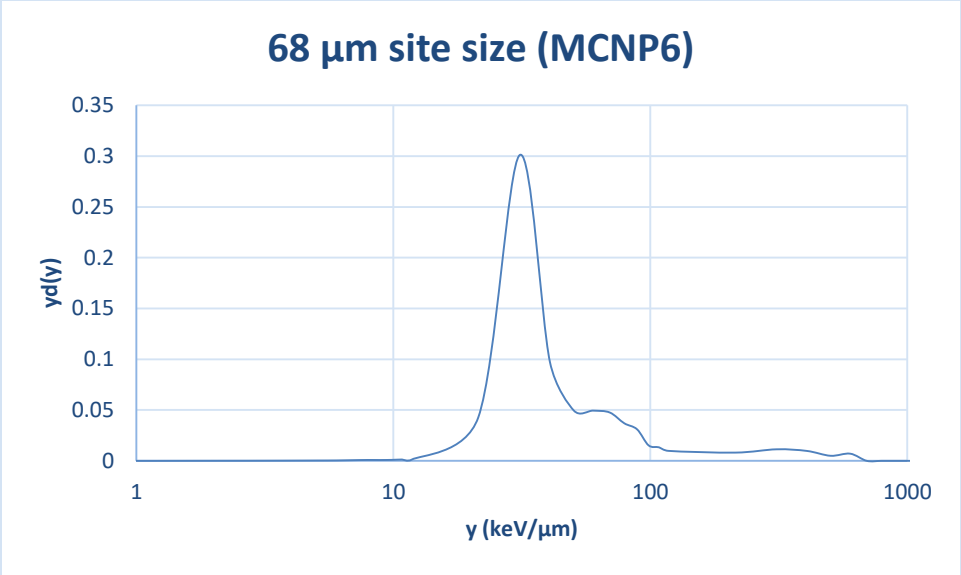

Figure 4.8 Lineal energy spectra for the 68 µm site size using the MCNP6 simulation.

The microdosimetric measurements for both site size is shown in table 4.2. These values are the calculated mean values taken from three measurements runs from each site size. There is a decrease in $\bar{y}_D$ as the site size increases. The decrease in $\bar{y}_D$ is probably related to the amount of energy transferred to the cavity by each kind of particle interaction mechanism. Most of the events are crossers, but at the neutron AmBe energy the three types of events starters, insiders, and stoppers become more important and frequently dominant over crossers for the heavy recoils particles. As the site size increases, these events deposit their energy, on average, in a distance less than the mean chord length, resulting in an underestimate for the microdosimetric parameters and a large decrease in the average quality factor Q. This is the reason why the dose equivalent for this relatively low energy neutron spectrum is underestimated by the 68 µm site size. Furthermore, the 2 µm show more events in the high lineal energy range

than the 68 μm sizes accompanied with lower fraction of deposited energy by low lineal energy events. This is due to the fact that this increase of diameter is not accompanied by more energy deposition, and therefore the spectrum is shifted toward lower lineal energy values. As observed from figure 4.2, the gas gain for the 2 μm diameter is higher than the gas gain for the 68 μm diameter. The more recoil protons present per unit dose having energies around the maximum in the stopping power curve, the sharper will be the proton drop point. The maximum average stopping power for the 2 μm diameter (100 keV/μm) is greater than the maximum average stopping power for the 68 μm diameter (27.5 keV/μm), therefore the proton drop point is higher for the 2 μm diameter.

The shape of the spectra between these two site sizes is not much different from each other except for the shift to the left due to the larger mean chord length. This is the dominant factor which determines the average energy deposited in the cavity and consequently the average quality factor.

Table 4.2 Microdosimetric parameters calculated for 2μm and 68 μm site size.

TEPC	Site Size	$\bar{y}_F$ (keV/μm)	$\bar{y}_D$ (keV/μm)	Avg. Quality factor Q
3.8 cm	2 μm	29.2	40.1	10.2
3.8 cm	68 μm	19.8	35.8	7.9

Table 4.3 shows that there is an excellent agreement between the calculated microdosimetric values from the experiments and the values calculated from the MCNP6 simulation. The difference in microdosimetric parameters $\bar{y}_F$, $\bar{y}_D$, and the average quality factor Q are not exceeding 10%. Any difference in the values, may be due to the accuracy of the cavity pressure and the calibration process.

Table 4.3 Microdosimetric parameters calculated from measured f(y) distributions for 2 µm and 68 µm site size compare with the MCNP6 calculated values.

TEPC	Site Size	$\bar{y}_F$	$\bar{y}_D$	Avg. Quality factor Q
3.8 cm	2 µm	29.2	40.1	10.2
MCNP6 Sim.	2 µm	27.3	43.5	11.1
Difference		**7.0%**	**8.5%**	**8.8%**
3.8 cm	68 µm	19.8	35.8	7.9
MCNP6 Sim.	68 µm	21.2	39.2	8.4
Difference		**7.1%**	**9.5%**	**6.3%**

Experimental uncertainties were measured for the microdosimetric values and are shown in table 4.4. Counting statistics accounted for the greatest uncertainty in the measuring of the microdosimetric values.

Table 4.4 Uncertainties in microdosimetric parameters for the 3.8 cm detector

Site Size	Runs	$\bar{y}_F$ (keV/µm)	$\bar{y}_D$ (keV/µm)	Avg. Quality factor Q
2 µm	1	28.7	41.1	10.3
2 µm	2	30.4	43.2	10.6
2 µm	3	28.5	36.1	9.8
Mean Value		29.2	40.1	10.2
Standard deviation σ		**±1.0**	**±3.6**	**±0.4**
68 µm	1	21.2	37.4	8.1
68 µm	2	19.2	36.9	7.9
68 um	3	19.0	36.1	7.7
Mean Value		19.8	36.8	7.9
Standard deviation σ		**±1.2**	**±1.7**	**±0.2**

These standard deviation values account for the greatest uncertainty in the measuring procedure and they represent a reasonable estimate of the overall uncertainty.

The absorbed dose was calculated using equation 4.10. This is the energy deposited by each individual event multiplied by the mean chord length and divided by the mass of the counter gas. The dose rate was then obtained by dividing the absorbed dose by six hours. The measurements in the lab with the AmBe source were taken over a period of six hours. The results are shown in table 4.5. There is only a small difference in the dose rate between the two diameters. The small difference is due to uncertainties in the measurements.

Table 4.5. 3.8 cm detector dosimetry for 2 µm and 68 µm site size

Site Size	Dose rate (mGy/hr.)	Equivalent Dose (mSv/hr.)	Avg. Quality Factor Q
2 µm	2.52	25.75	10.22
68 µm	2.28	18.08	7.93

For the relatively low energy AmBe neutrons spectrum the equivalent dose for the 68 µm site size was much lower than the equivalent dose for the 2 µm site size by a 1.25 factor. The equivalent dose H, is the product of the absorbed dose and the average quality factor. The equivalent dose depends on the quality factor and it is used by health physicist and radiobiologist to estimate the radiation damage in a cell. The results in table 4.4 clearly shown the 68 µm site size underestimated the equivalent dose when using an AmBe source of neutron average energy of 4.5 MeV. In section 4.4 a Monte Carlo simulation of GCR very high energy particles (H, He, heavy ions) demonstrated how simulating a 68 µm site size does not underestimate the equivalent dose in space.

4.3.3 The 1.8 cm diameter detector

The results for the 1.8 cm detector will be discussed in this section. Figure 4.9 shows the microdosimetry event size spectra for the 2 µm site size. The proton peak is found around 38.5 KeV/µm. The peaks around the proton edge area, the high lineal energy side of the spectra, are more visible than with the same spectra from the 3.8 cm detector (Figure 4.4). This could be because of less electronic noise with the 1.8 cm

detector than with the 3.8 cm detector, which results in a better resolution. Since the 1.8 cm diameter detector is smaller than the 3.8 cm diameter detector, the pre-amplifier circuit board is of course smaller for the 1.8 cm detector. The revised component layout and the added electromagnetic shielding to the detector, provided by the gold plated aluminum vacuum chamber, providing for a better resolution.

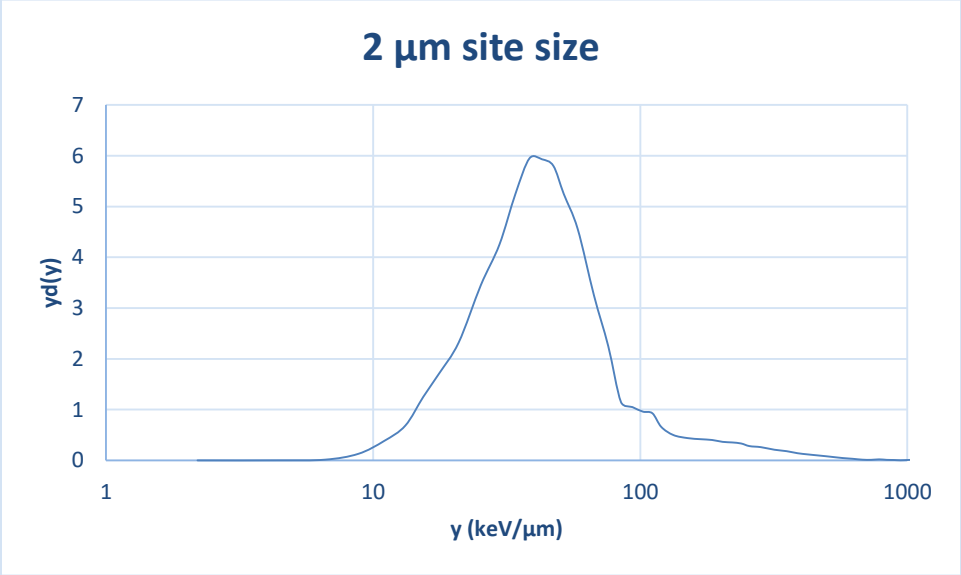

Figure 4.9 Lineal energy spectra for the 2 µm site size measured with the 1.8 cm detector.

The spectrum simulated using MCNP6 code is shown in figure 4.10. The proton peak is found around 36.8 keV/µm which is close to the 38.5 keV/µm peak found in the experimental spectra. Once again it is important to note that the small peaks found between 1 keV/µm and 10 keV/µm are more visible in the simulation than the experimental spectra.

The lineal energy spectra of the 32 µm site size is shown in figure 4.11. The proton peak is around 35.1 keV/µm. The peak found here is narrower than the peak for the 2 µm site size due to the reduced energy loss straggling. Also, the proton peak for the 2 µm site size is higher than the 32 µm site size. The differences in spectra were the same as for the 3.8 cm detector, except for the better resolution for the 1.8 cm detector which defined a more visible high energy tail peaks.

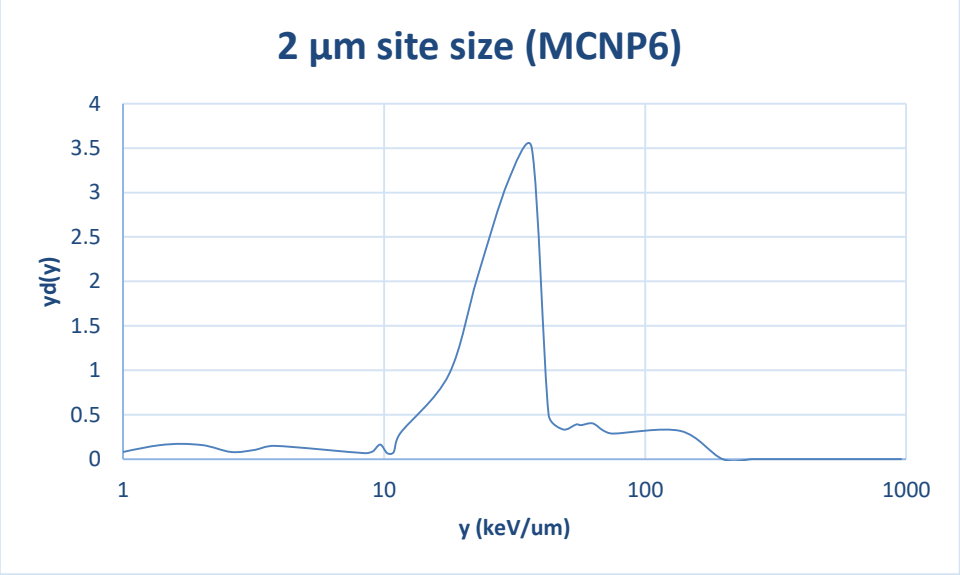

Figure 4.10 Lineal energy spectra for the 2 µm site size using the MCNP6 simulation.

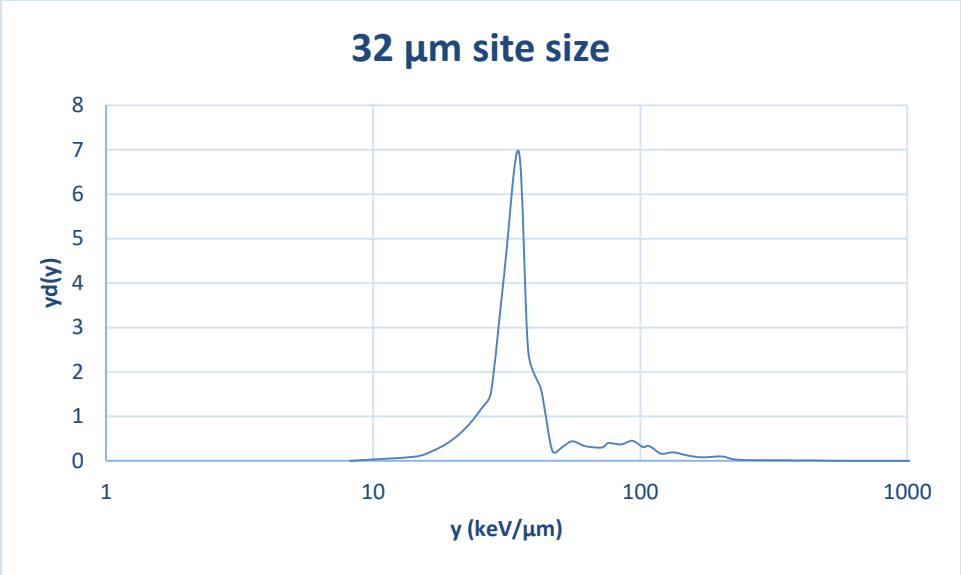

Figure 4.11 Lineal energy spectra for the 32 µm site size measured with the 1.8 cm detector.

The change in the shape of the spectra for the two site sizes is shown in figure 4.12. The 32 µm site size has a narrow peak which presents a better resolution than the 2 µm site size peak. As expected the lineal energy y spectra shift to lower values as site size increases. As observed from figure 4.10, we can compare the high lineal energy peaks and notice more visible small peaks and a sharper proton drop point for the 32 µm site size. Using this smaller diameter detector simulating a 32 µm site size proved to be very useful compared using the larger diameter detector. The resolution is better than the 2 µm site size and there is improvement in the variance indicated by the narrower peak.

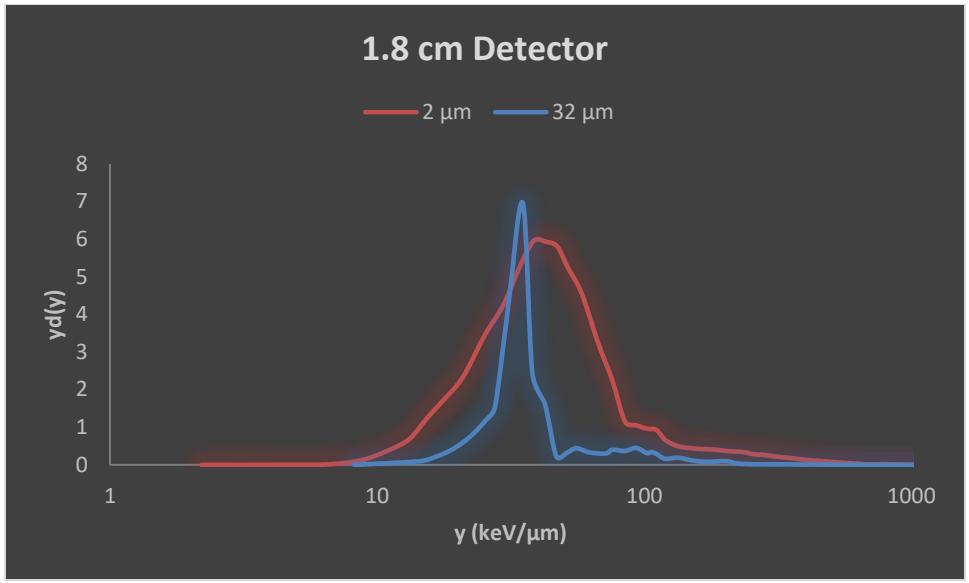

Figure 4.12 Lineal energy spectra for the two site sizes for the 1.8 cm Detector.

The lineal energy spectra for this simulation is shown in figure 4.13. The proton peak maximum is around 34.3 keV/µm. The experimental and simulation spectra proton peak and proton drop point appear around the same location in the energy spectra. Using the MCNP6 simulation was a good tool not only to predict the behavior of these two detectors in a radiation field but also to be able to locate the proton drop point which can be used in an experimental set up to calibrate the detector.

The microdosimetric measurements for both site size is shown in table 4.6. The 32 µm site size showed a decrease in all values when compare with the 2 µm site size. The same situation was observed for the 3.8 cm detector. Here again we noticed the average quality factor is much smaller for the larger site size. When using this smaller diameter detector the dose equivalent is underestimated by the 32 µm site size, just as

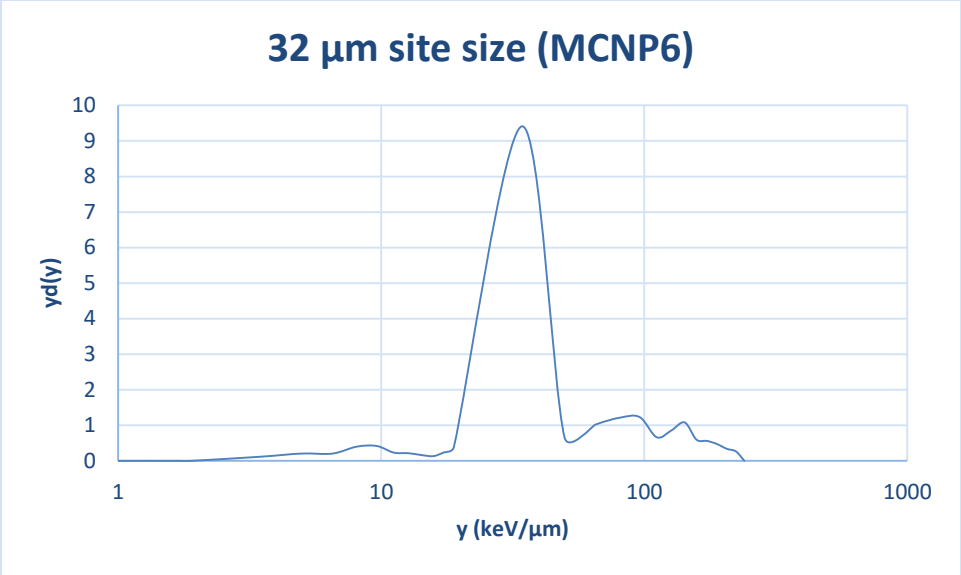

Figure 4.13 Lineal energy spectra for the 32 µm site size using the MCNP6 simulation.

the larger diameter detector underestimate the dose equivalent for the 68 µm site size. We can conclude that for a relatively low energy neutron spectrum, the average quality factor decreases as the site size increases. In section 4.3.4 it will be demonstrated with MCNP6 simulation that for GCR high energy particles the larger site size does not underestimate the dose equivalent.

Table 4.6 Microdosimetric parameters calculated for 2µm and 32 µm site size.

TEPC	Site Size	$\bar{y}_F$ (keV/µm)	$\bar{y}_D$ (keV/µm)	Avg. Quality factor Q
1.8 cm	2 µm	26.4	40.8	9.9
1.8 cm	32 µm	18.2	37.1	8.2

The microdosimetric values calculated from the MCNP6 simulation are shown in table 4.7. In this table the simulation results are compared with the experimental results from table 4.6. The difference in the microdosimetric parameters are not exceeding 11%. This is a good approximation taking into consideration the accuracy of the cavity pressure and the calibration process.

Table 4.7 Microdosimetric parameters calculated from measured f(y) distributions for 2 µm and 32 µm site size compare with the MCNP6 calculated values.

TEPC	Site Size	$\bar{y}_F$	$\bar{y}_D$	Avg. Quality factor Q
1.8 cm	2 µm	26.4	40.8	9.9
MCNP Sim.	2 µm	28.4	45.4	10.9
Difference		**7.5%**	**11.3%**	**10.1%**
1.8 cm	32 µm	18.2	37.1	8.2
MCNP6 Sim.	32 µm	19.5	41.2	9.0
Difference		**7.1%**	**11.1%**	**9.8%**

The absorbed dose for the 6 hour exposure in the experimental geometry described previously was calculated for both site sizes using equation 4.10 in order to illustrate the effect of site size. This was done using the pulse height distribution. The lineal energy "y" was multiplied by the mean chord length to get the energy deposited in the cavity. This was then divided by the mass of the counter gas to get the total absorbed dose. The measurements in the lab with the AmBe source were taken over a period of six hours for each run and the distance of the detector from the source was 15 cm. The dose rate was then obtained by dividing the absorbed dose by six hours. The results are shown in table 4.8. Measuring the absorbed dose is a difficult task because of a number of uncertainties involved when working with the detector under different pressures.

Table 4.8. 1.8 cm detector dosimetry for 2 μm and 32 μm site size.

Site Size	Dose rate (mGy/hr.)	Equivalent Dose (mSv/hr.)	Avg. Quality Factor Q
2 μm	0.75	7.43	9.91
32 μm	0.66	5.44	8.24

The large sites do not meet cavity theory requirements so they are expected to underestimate dose and the error should be larger for 68 μm site size. There is also the uncertainty in the detector distance from the source; how accurate is the distance measured when moving the detector for each run. Considering these factors, the dose rate calculated for both site sizes shown in table 4.8 is a good approximation of the dose rate calculated by a larger site size using the 1.8 cm detector at atmospheric pressure.

4.4 MCNP6 simulation for GCR with 3.8 cm diameter & 1.8 cm diameter detector

The results for the MCNP6 simulations of GCR incident particles are discussed in this section. The calculations were performed for protons (H), helions (He), and iron (Fe) ions. The energies used were 1000 MeV/nucleon for each particle and the Badhwar-O'Neill 2014 Galactic Cosmic Ray distribution. The Badhwar-O'Neill (BON) Galactic Cosmic Ray flux model is based on GCR measurements from particle detectors. This model is used by NASA for the analysis of radiation health risks to astronauts in space missions (O'Neill, 2015). The model is used to describe relevant spectra of particles and energies appearing in deep space. The diameters of the simulated sites

were 2, 32, and 68 μm. The detectors were filled with propane gas at low and atmospheric pressure.

As mentioned before protons are the more abundance particles in the GCR spectrum with about 90% of total particles but iron ions which are less than 1% contribute more to the equivalent dose. This is because the LET is roughly proportional to the square of the particle charge. In order to be able to compare the effect of each particle (H, He, Fe) on both detectors, each particle spectrum was analyzed separately and the microdosimetric parameters of each particles were calculated.

4.4.1. 1000 MeV/n Proton, Helium, and Iron Spectra

Proton and helium particles have much smaller LET than iron ion particles. This is due to the particle charge. The LET is roughly proportional to the square of the particle charge. Figure 4.14 shows the frequency distribution of events produced by 1000MeV/n protons in different site sizes for the 3.8 cm detector. The most probable y is 0.40 and 0.32 keV/μm for 68 and 2 μm site sizes respectively. The peak shifts to the left as the site size decreases. Figure 4.15 shows the frequency distribution events produced by 1000 MeV/n helium's particles in different site sizes for the 3.8 cm detector. Helium has a charge of 2^+ resulting a LET 4 times higher than that of proton, causing its peak shift to the right of the proton peak. The most probable y is 1.5 and 1.4 for 68 and 2 μm site sizes respectively.

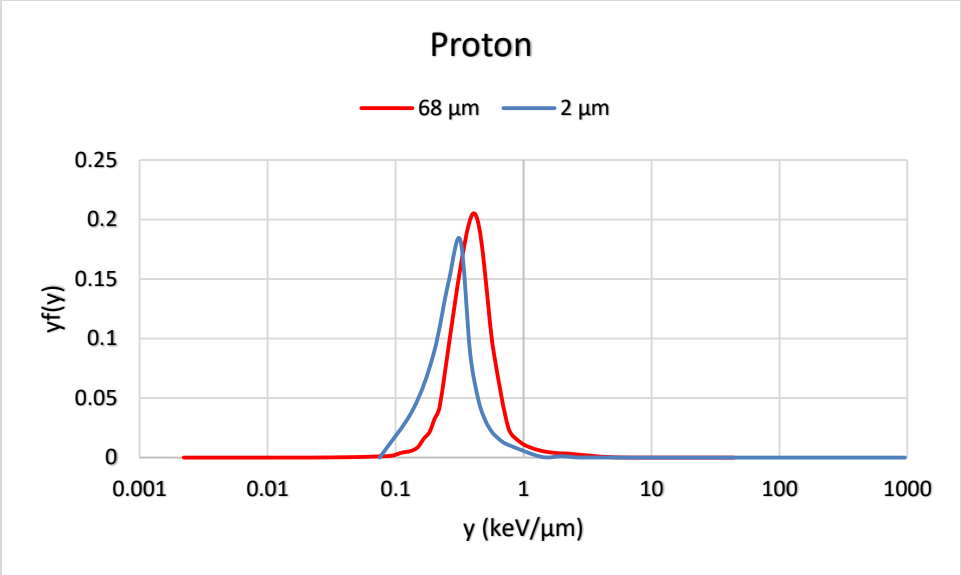

Figure 4.14 Frequency distribution spectra of 1000 MeV/n protons for simulating sites 2 µm and 68 µm for the 3.8 cm detector.

The 68 µm site size "y" value is slightly higher than the 2 µm site size which is expected because the larger site includes more of the energy deposited by delta rays. The frequency distributions produced by 1000 MeV/n iron ions is shown in figure 4.16. The most probable y is 338 and 321 keV/µm for 68 and 2 µm site sizes respectively. The 68 µm site size is narrower and more defined than the 2 µm peak, but overall the shape of the two peaks are very similar. The largest site sizes has the largest average number of delta ray events, therefore for the largest sites the contribution of delta rays increases and the results will deviate from the z^2 relationship.

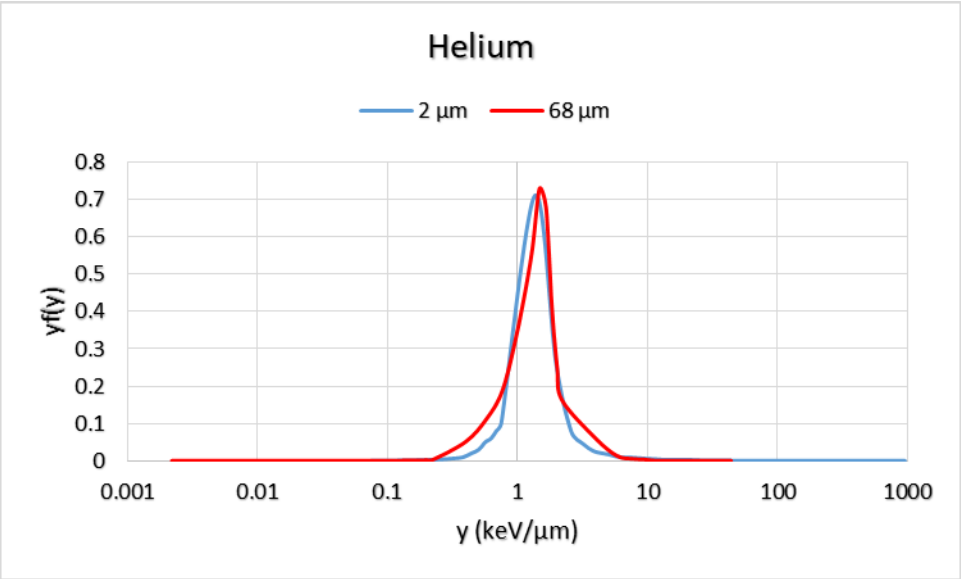

Figure 4.15 Frequency distribution spectra of 1000 MeV/n helions for simulating sites 2 µm and 68 µm for the 3.8 cm detector.

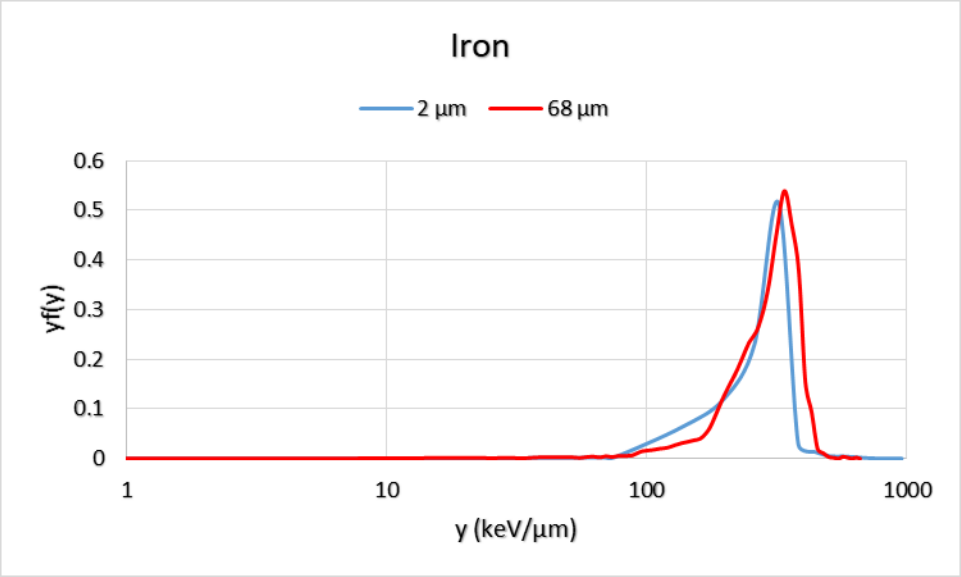

Figure 4.16 Frequency distribution spectra of 1000 MeV/n irons for simulating sites 2 µm and 68 µm for the 3.8 cm detector.

Usually protons and delta ray events produced by heavy ions, in this case iron particles, are hard to separate. The wall effect will cause more energy to be deposited in the site by delta ray events than would occur in a wall-less detector.

In figure 4.17 the dose distribution "yd(y)" for single 1000 MeV/n proton, helium, and iron particles is shown. As expected the iron particles dominated the spectrum for the dose distribution to the extent that proton and helium events are not visible. The most probable y is 339 and 322 for 68 and 2 μm site sizes respectively. There appears to be excellent agreement between the two event size spectra with a slightly greater dose mean lineal energy for the 68 μm site size.

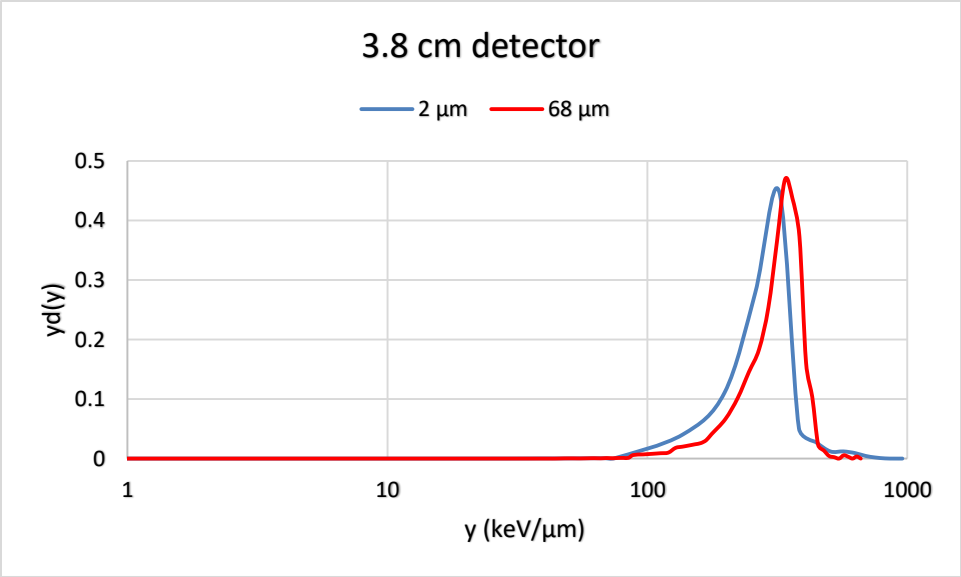

Figure 4.17 Dose distribution spectra of 1000 MeV/n protons, helions, and iron simulating sites 2 μm and 68 μm for the 3.8 cm detector.

The microdosimetric parameters for each particle and the spectrum in figure 4.17 are shown in table 4.9. Here we can see the relationship between $\bar{y}_F$, $\bar{y}_D$, and LET. The $\bar{y}_F$ was always less than LET of the three incident particles. On the other hand, $\bar{y}_D$ was slightly less than LET for iron particles but greater than LET for proton and helium particles. This is due to detector resolution and energy straggling that increases the relative number of events with large energy deposition. These large events have a significant impact on the dose distribution and mean. The average quality factor for proton and helium is close to 1 as expected and increases rapidly to around 18 for the more energetic and penetrating iron particles. This influence of iron ions is seen in the plot of "yd(y) vs y" shown in figure 4.17 where the single event spectra for all three particles have been added together just as you will find in the GCR spectrum. This influence is mostly seen in the large value of $\bar{y}_D$ relative to $\bar{y}_F$, and the high average quality factor for the three particles together shown in table 4.9.

The average quality factor Q for the 2 and 68 μm site sizes is 17.98 and 17.78 respectively. The average quality factor Q for the three particles together was calculated by taking the sum of the dose equivalent of the three particles and dividing by the sum of the dose of the three particles. The larger site size estimation of the average quality factor Q was very similar to the smaller site size and did not underestimate the dose equivalent. Under the very high energy of 1000 MeV/n considered here, there were a lot of crossers particles and not many stoppers which contributed to larger deposition energy deposited in the larger site size.

Table 4.9. Microdosimetric parameters for 1000 MeV/n proton, helium, and iron particles for the 3.8 cm detector.

Particle	Site Size	$\bar{y}_F$	$\bar{y}_D$	LET	Avg. Quality factor
Proton	2 μm	0.28	0.38	0.32	1.01
	68 μm	0.39	0.52	0.40	1.02
Helium	2 μm	1.2	2.0	1.4	1.08
	68 μm	1.5	2.3	1.5	1.09
Iron	2 μm	248	307	321	18.12
	68 μm	260	332	338	17.92
Proton, Helium, and Iron	2 μm	88	273		17.98
	68 μm	94	302		17.78

The 1.8 cm detector characteristics simulated under 1000 MeV/n proton, helium, and iron particles are discussed below. This is a smaller diameter detector and a thinner wall thickness than the 3.8 cm detector. Nevertheless we would expect a similar behavior under the influence of high GCR particles as the 3.8 cm detector. The main difference between these two detectors is when the counter gas is at atmospheric pressure, we get 32 and 68 μm simulated site size for 1.8 and 3.8 cm detector respectively. Figure 4.18 shows the frequency distribution of events produced by 1000MeV/n protons in different site sizes. The most probable y is 0.35 and 0.31 keV/μm for 32 and 2 μm site sizes respectively. Figure 4.19 shows the frequency distribution events produced by 1000 MeV/n helium in different site sizes. The most probable y is 1.44 and 1.39 keV/μm for 32 and 2 μm site sizes respectively. The lineal energy increases as the site size increases.

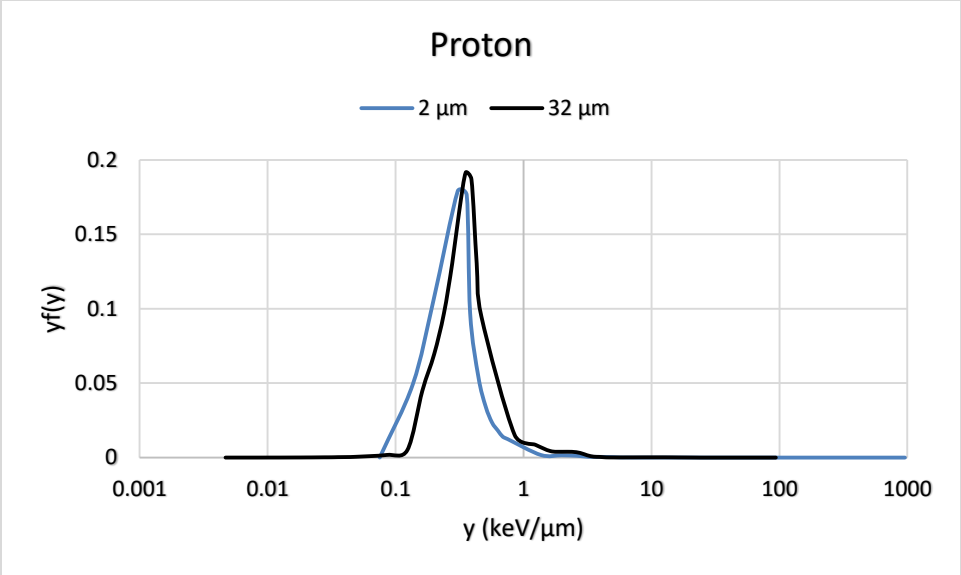

Figure 4.18 Frequency distribution spectra of 1000 MeV/n protons for simulating sites 2 µm and 32 µm for the 1.8 cm detector.

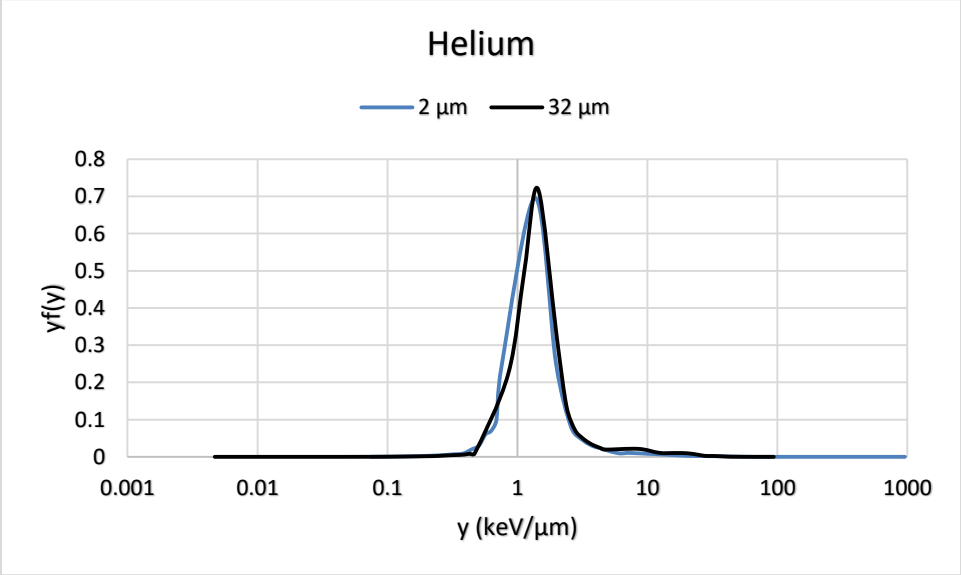

Figure 4.19 Frequency distribution spectra of 1000 MeV/n helions for simulating sites 2 µm and 32 µm for the 1.8 cm detector.

The frequency distributions produced by 1000 MeV/n iron ions are shown in figure 4.20. The most probable y is 332 and 321 keV/μm for 32 and 2 μm site sizes respectively. The 32 μm site size peak is narrower than the 2 μm peak with a better defined sharp edge at the end of the lineal energy spectrum due to energy straggling.

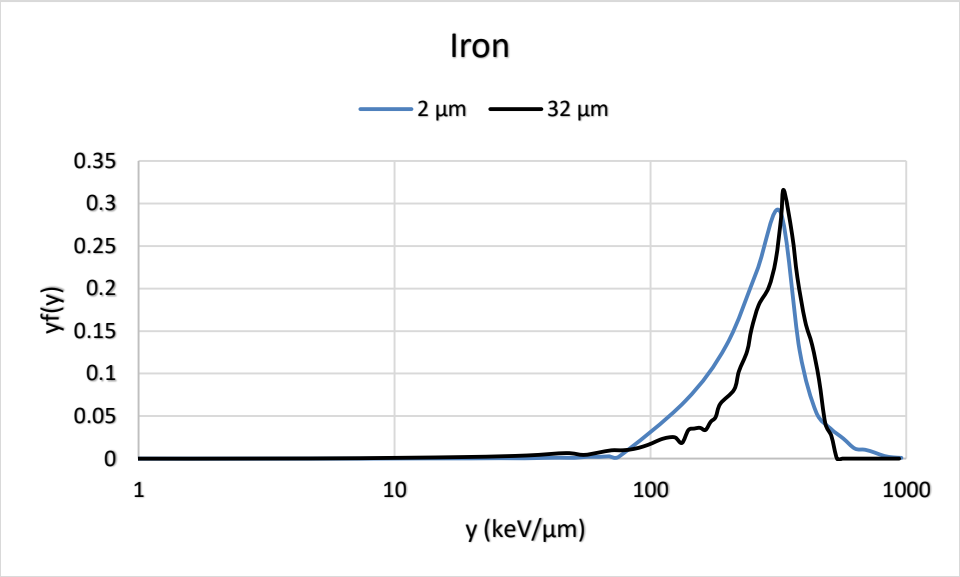

Figure 4.20 Frequency distribution spectra of 1000 MeV/n irons for simulating sites 2 μm and 32 μm for the 1.8 cm detector.

The dose distribution "yd(y)" plot is shown in figure 4.20. The most probable y is 334 and 323 keV/μm for 32 and 2 μm site size respectively. This spectra mirror the spectra from figure 4.19 which confirmed once again the dominant of iron particles for the dose distribution. This is evidence why the study of the effect of iron particles is very important in radiation biology. The next subsection simulated the Badhwar-O"neill 2014 GCR flux model for a more realistic GCR particles spectra in deep space.

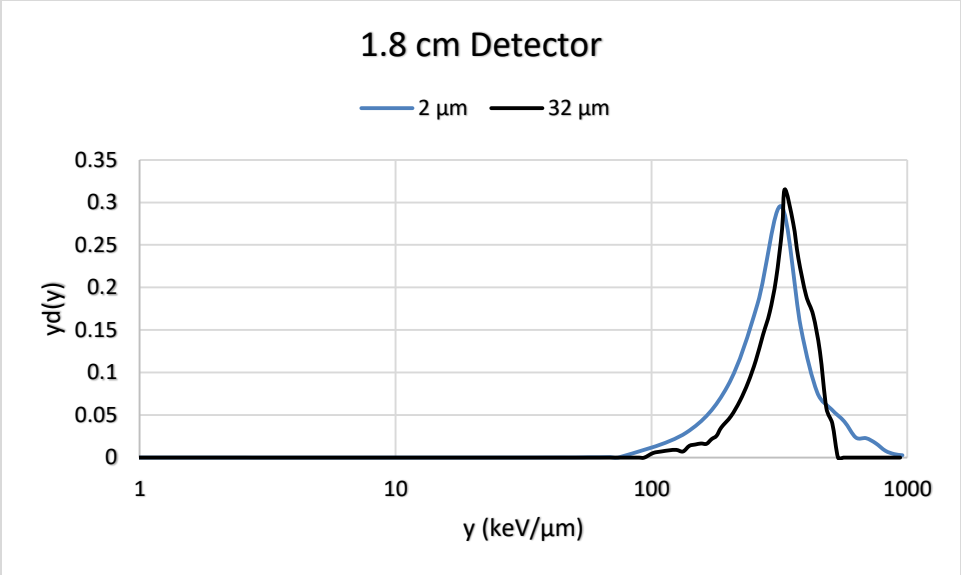

Figure 4.21 Dose distribution spectra of 1000 MeV/n protons, helions, and iron simulating sites 2 µm and 32 µm for the 1.8 cm detector.

The microdosimetric parameters for each particle and the spectrum in figure 4.21 is shown in table 4.10. The average quality factor Q for the 2 and 32 µm site sizes is 17.91 and 17.83 respectively. The larger site size estimation of the average quality factor Q was very similar to the smaller site size with a difference less than 0.05% compare with more than 28% when using low energy AmBe source.

Table 4.10. Microdosimetric parameters for 1000 MeV/n proton, helium, and iron particles for the 1.8 cm detector.

Particle	Site Size	$\bar{y}_F$	$\bar{y}_D$	LET	Avg. Quality factor
Proton	2 µm	0.24	0.35	0.26	1.01
	32 µm	0.33	0.43	0.35	1.01
Helium	2 µm	1.35	2.11	1.37	1.08
	32 µm	1.42	2.14	1.44	1.08
Iron	2 µm	262	316	321	18.04
	32 µm	270	323	332	17.96
Proton, Helium, and Iron	2 µm	90	314		17.91
	32 µm	96	318		17.83

4.4.2. Badhwar-O'neill 2014 GCR flux model distribution

To better describe the behavior of a TEPCs when submitted to GCRs particles, a set of energy ranges for representative particles is described here. Last section described the behavior of a TEPC in deep space using three different incident particles under one energy 1000 MeV/n. In reality, incident particles are not mono-energetic, but their energy is distributed within some range. This section describes the behavior of a 3.8 cm and 1.8 cm diameter detector exposed to charged particle energy spectra characteristic of GCRs in deep space. The Badhwar-O'neill (BON) model was used to generate the GCR source incident on both detectors in deep space. The data presented in table 4.10 are fractional abundances of proton, helium, and iron incident particles divided into energy groups. This data is presented in the BON model as effective dose and was converted to relative abundances by using the effective dose-flux relationship equation:

$$E = \phi \frac{dE}{dX} \; Q\left(\frac{dE}{dX}\right) \tag{4.13}$$

Where E is the effective dose which is equal to dose equivalent H for uniform whole body irradiation. The flux is denoted by ϕ and $\frac{dE}{dX}$ is the stopping power. The average quality factor Q is used as a function of stopping power. Table 4.11 is the relative abundance of protons, helions, and irons behind 20 g/cm^2 aluminum shielding at solar minimum. Aluminum shielding thickness between 20-30 g/cm^2 is usually used by spacecraft to achieve structural and payload requirements and keep the dose equivalent to a minimum. For greater than 30 g/cm^2 thickness, dose equivalent increases due to

secondary neutron and light particle production. The energy groups between 0.5 GeV and 20 GeV accounts for most of the fluence for all ions. Protons are the most abundant of all three incident particles in all energy groups with a total of 95.48% and irons are the least with 0.0014%.

Table 4.11. Relative abundance of the indicated energy range for protons, helions, and iron incident particles behind 20 g/cm^2 aluminum shielding at a period of solar minimum activity.

Particle	0-.250 GeV/n	.250-.500 GeV/n	.500-1.5 GeV/n	1.5-4.0 GeV/n	4.0-20.0 GeV/n	Total (%)
Proton	1.98	8.89	29.96	30.29	24.36	95.48
Helium	0.45	0.82	1.53	1.09	0.62	4.51
Iron	0.0000125	0.0000125	0.000593	0.000477	0.000263	0.0014
Totals	2.43	9.71	31.49	31.38	24.98	**100.00**

The energy distribution in table 4.11 was implemented in the MCNP6 codes to get a new spectrum for the proton, helium, and iron incident particles. In figure 4.22 the frequency distribution yf(y) of proton, helium, and iron particles for a 2 μm site size is shown. The proton and helium incident particle frequency mean lineal energies are the same as were found for the mono-energetic simulated spectrum in section 4.4.1. The iron incident particle most probable y of 137 keV/μm is much less than the 321 keV/μm for the mono-energetic simulated spectrum. This is because the Badhwar-O'neill GCR distribution include energies as high as 20 GeV/n which are much larger than the 1 GeV/n and the stopping power of particles decreases in this energy range.

The dose distribution yd(y) of proton, helium, and iron incident particles for a 2 μm site size is shown in figure 4.23. Here we can see that iron particles make up significant fraction of the GCR spectrum and contribute most to dose equivalent. We

can conclude although iron particles are only a tiny fraction of the GCR spectrum, their contribution to the GCR dose is substantial. There are other HZE particles such as carbon and silicon that contributes to the GCR total dose, but iron is the most important because of its relative contribution to the GCR dose and its high LET.

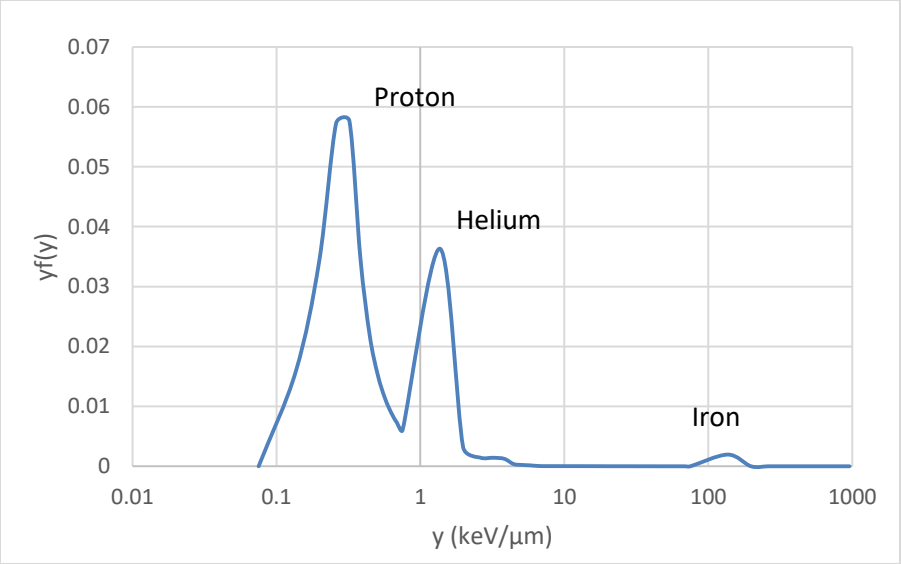

Figure 4.22. Frequency distribution spectra of the Badhwar-O'neill model simulating site 2 µm with the 3.8 cm detector.

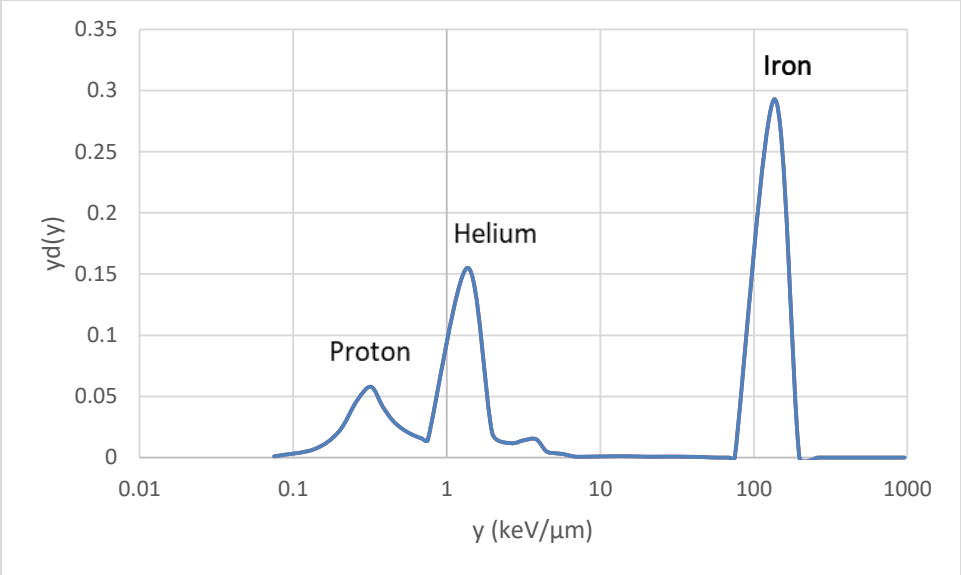

Figure 4.23. Dose distribution spectra of the Badhwar-O'neill model simulating site 2 µm with the 3.8 cm detector.

The spectrum for the 32 µm and 68 µm site sizes is for the most part similar to the 2 µm site size with the exception of the helium peak which opens wider in the energy spectrum between 4 keV/µm and 43 keV/µm. In the large site some of the alpha particles slow down significantly, therefore presenting a higher average LET. Also, the fragmentations particles created from the nuclear reaction with the aluminum shielding contributed to the higher y value for the helium peak. This spectrum is shown in figure 4.24 for the "yf(y)" plot and figure 4.25 for the "yd(y) plot. The most probable y is 0.31, 8.5, and 141 keV/µm for the proton, helium, and iron particle respectively in a simulated 32 µm site size.

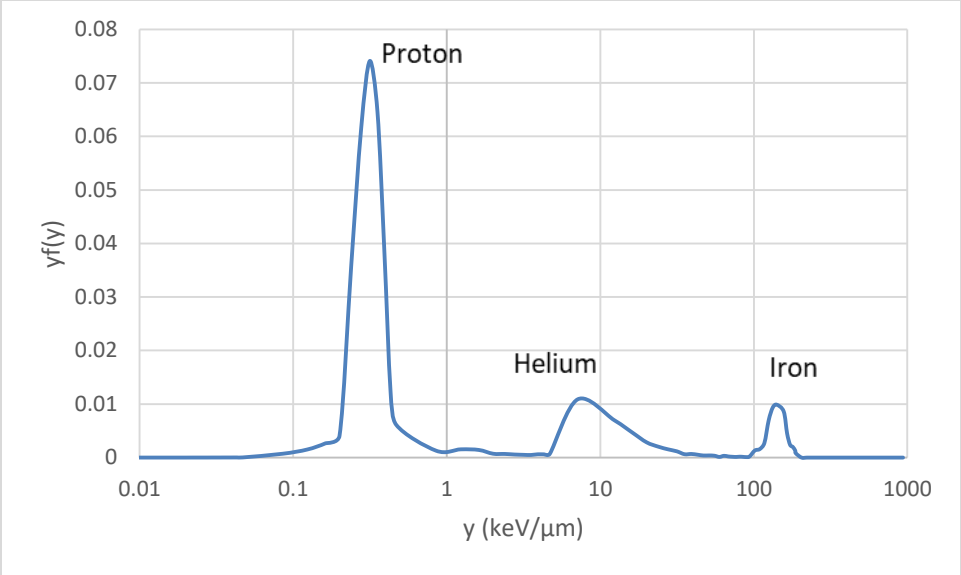

Figure 4.24. Frequency distribution spectra of the Badhwar-O'neill model simulating site 32 µm with the 1.8 cm detector.

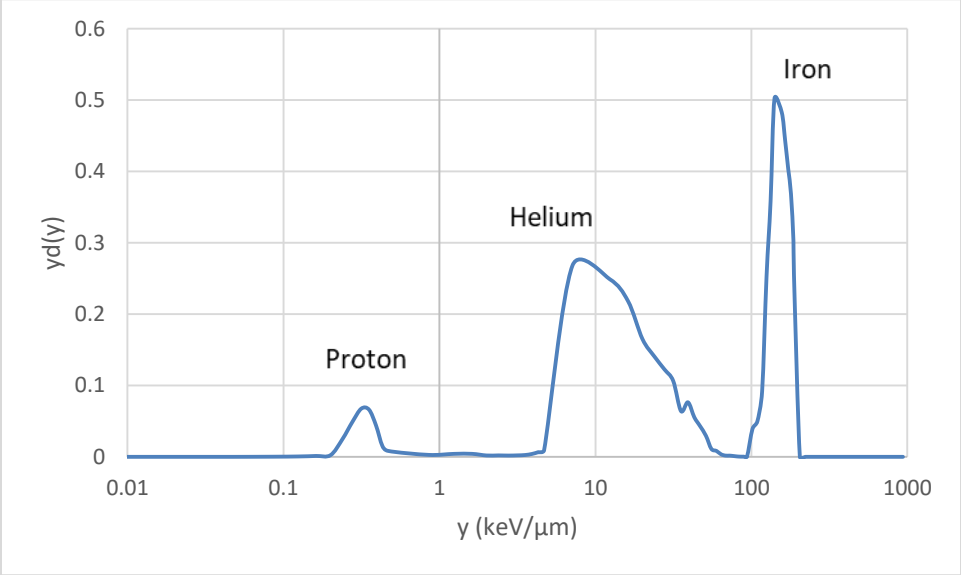

Figure 4.25. Dose distribution spectra of the Badhwar-O'neill model simulating site 32 µm with the 1.8 cm detector.

Figure 4.26 and 4.27 shows the spectrum for the 68 μm site size. The most probable y is 0.40, 7.6, and 144 keV/μm for proton, helium, and iron particle respectively. Some of the lower energy helium ions stop in the larger site resulting in the decrease in $\bar{y}_F$ and $\bar{y}_D$. The 68 μm site size provided very similar results overall when compared with the 32 μm site size. The impact of solar activity on these results appears to be small even at small shielding thickness. During solar minimum, the relative contribution to dose equivalent from iron particles increased at a greater factor than proton and helium.

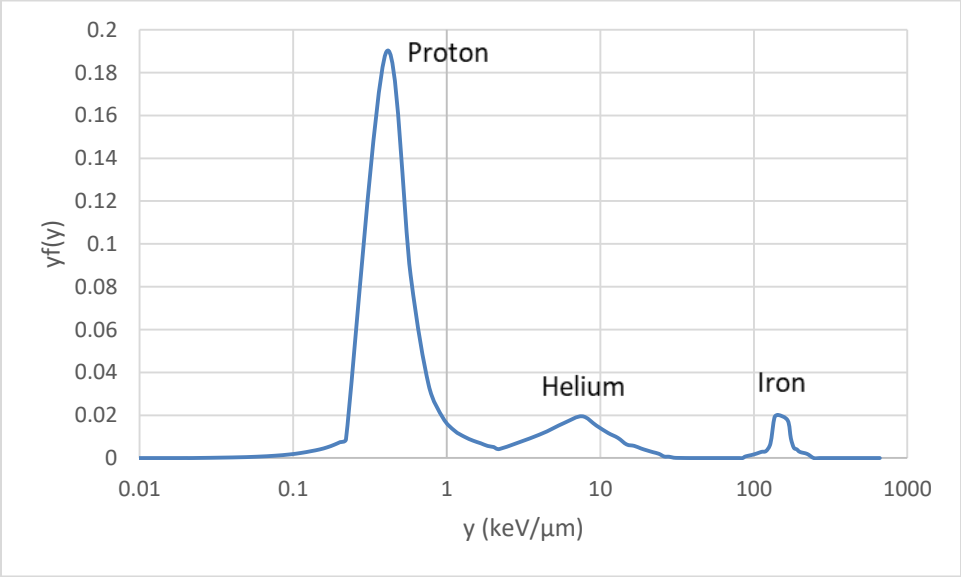

Figure 4.26. Frequency distribution spectra of the Badhwar-O'neill model simulating site 68 μm with the 3.8 cm detector.

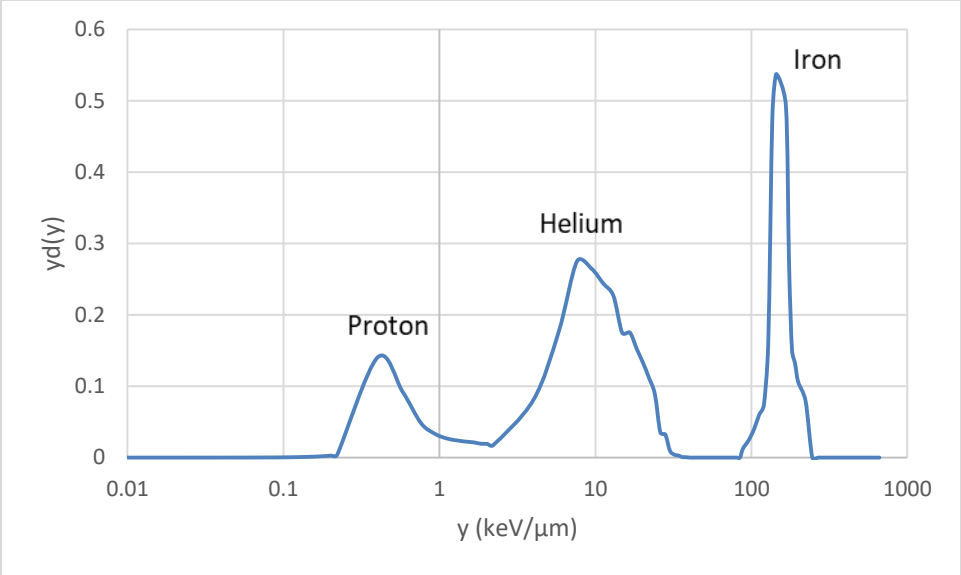

Figure 4.27. Dose distribution spectra of the Badhwar-O'neill model simulating site 68 µm with the 3.8 cm detector.

The Badhwar-O'neill flux model is a more realistic exposure approach to an astronaut because it is behind a 20 g/cm^2 aluminum shielding. Moreover, the 1000 MeV/n particles are in free deep space with no shielding. Therefore we expect the astronaut's exposure to free deep space and no shielding to be far more dangerous to their health than the one with shielding. This can be seen by looking at the "yd(y)" plots in figure 4.17 and 4.21 where the iron particles which are more penetrating and higher LET than proton and helium particles completely dominated the lineal energy spectrum.

The microdosimetric parameters for the simulated Badhwar-O'Neill model is show in table 4.12. The average quality factor Q for the 2, 32 and 68 µm site sizes is 1.15, 1.27 and 1.31 respectively.

Table 4.12. Microdosimetric parameters for the simulated Badhwar-O'neill model for the 2, 32 and 68 μm site size.

Simulation model	TEPC	Site Size	$\bar{y}_F$	$\bar{y}_D$	Avg. Quality factor Q
Badhwar-O'Neill	1.8	2 μm	0.31	1.39	1.15
	3.8	2 μm	0.32	1.36	1.15
	1.8	32 μm	0.43	4.07	1.27
	3.8	68 μm	0.53	5.29	1.31

For the 1000 MeV/n simulation the average quality factor Q was 17.98, 17.83 and 17.78 for the 2, 32 and 68 μm site sizes. The higher average quality factor for the 1000 MeV/n simulation is due to the higher fraction of the absorbed dose delivered by the iron particles. The higher $\bar{y}_D$ relative to $\bar{y}_F$ is due because of the influence of iron particles. Here we can see the difference in the average quality factor of both simulated models. Since the Badhwar-O'neill model is based on exposure to GCRs behind an aluminum shielding, it makes sense to conclude that its average quality factor is much lower than the 1000 MeV/n model in free space with no shielding.

CHAPTER V

CONCLUSIONS AND FUTURE WORKS

5.*1. Conclusions*

The three main objectives of this study were achieved through the calculation of frequency-mean lineal energy, dose-mean lineal energy, and average quality factor of simulated space radiation using 3.8 and 1.8 cm diameter detectors that operate at atmospheric pressure. This study also determined the gas gain and evaluated the characteristics of both detectors at low and atmospheric pressure to determine the feasibility to measure absorbed dose and dose equivalent in space. The data generated by using the Monte Carlo simulation offer insight into the behavior of both detectors in free space shielded and unshielded scenarios.

The gas gain was higher at a lower counter gas pressure than at atmospheric pressure for both detectors due to electron mobility around the anode wire. But this is not a disadvantage when using 32 and 68 μm site size because the energy imparted at these site sizes is much greater than at 2 μm site size, so a lower gas gain will result in the same signal to noise level and allow detection of low LET events. The gas gain as a function of voltage presented an almost linear behavior as expected using propane based tissue gas. This behavior was observed for each 2, 32, and 68 μm site size. The objective was achieved by showing that both detectors can performed at atmospheric pressure with the same sensitivity that they performed at low pressure.

In terms of microdosimeters parameters there was a decrease in $\bar{y}_D$ as the site size increases when the detector is irradiated using the AmBe source. With the AmBe neutron spectrum, the starter, insider, and stopper events become significant components of the charged particle spectrum responsible for energy deposition. As the site size increases, these events deposit their energy, on average, in a distance less than the mean chord length, resulting in an underestimate in the average quality factor when using the larger site sizes. The larger sites do not meet cavity theory requirements so they are expected to underestimate dose and the error was shown to be larger for 68 μm site size, as expected.

The simulated GCRs particles offered additional insight into the distribution of energy deposition events in deep space and how both detectors performed under low and atmospheric pressure. A comparison of lineal energy spectra produced by the free space unshielded 1000 MeV/n particles and the Badhwar-O'Neill shielded flux model shows the difference in the influence of HZE ions in the spectra. The proton and iron particles of the Badhwar-O'Neill model has a lower average LET than the 1000 MeV/n particles because some primary particles with higher velocity and therefore have lower LET.

Finally, under the HZE ions of the GCR spectrum there were a lot of crossers particles and not many stoppers so energy deposited increased with increasing site size. Consequently the larger site sizes 32 and 68 μm produce estimates of the average quality factor that differ by less than 1% from those produced by the 2 μm site size. Both, 3.8 and 1.8 cm detectors, operating at atmospheric pressure will produce dosimetry results essentially identical to those produced by a 2 μm site in the space radiation environment.

5.2. Future Works

While the use of two TEPCs, working under atmospheric pressure, to determine the average quality factor of GCR particles was evaluated, this was done using Monte Carlo simulations. Monte Carlo simulation is always a good starting point of any study involving radiation environment, especially when that environment is not readily available in the lab. Nevertheless it is always of great benefit to compare the simulation results with experimental results to have a better understanding of how the TEPC will behave in a radiation environment. Therefore an effort to test the two detectors exposed to HZE particles using a heavy ion accelerator is recommended. Before the detector is ready to go into deep space, which may take years, it is recommended to test it using a heavy ion medical accelerator or a facility lab with a fast ion accelerator with beam energies from 100 to 1000 MeV/n. It is therefore possible to design experiments studying the same ions involved in this study and modeling the primary particles in the space radiation environment.

Furthermore, it will be beneficial to add simulations including solar events and other galactic cosmic rays. In the present study only proton, helium, and iron particles were considered. Other GCRs particles such as carbon and silicon should be part of future studies. Solar events deliver significant doses to humans in deep space, but determining a proper procedure to measure a solar event is difficult because of random energies and intensities of recorded events.

REFERENCES

American Association of Physicist in Medicine. "Protocol for neutron beam dosimetry". New York, NY. AAPM Report No. 7; 1980.

Arshak, K. and Korostynska, O. "Advanced Materials and Techniques for Radiation Dosimetry". Norwood, MA: Artech House Inc; 2006.

Berger, M.J., Coursey, J.S., Zucker, M.A, and Chang, J. "Stopping-Power & Range Tables for Electrons, Protons, and Helium Ions." Available at: https://www.nist.gov/pml/stopping-power-range-tables-electrons-protons-and-helium-ions. Accessed 15 September 2017.

Braby, L.A., Johnson, G.W., and Barthe, J. "Practical Considerations in the Design and Construction of Tissue-Equivalent Proportional Counters". Radiation Protection Dosimetry, Vol. 61, pp. 351-379; 1995.

ePlastics. "Acetal Delrin Plastic". ePlastics Company, 1998. Available at: http://www.eplastics.com/Acetal_Delrin?utm_source. Accessed 11 September 2017.

Farahmand, M. "A novel tissue-equivalent proportional counter based on a gas electron multiplier". Delft, The Netherlands. Delft University Press Science; 2004.

Hall, E.J. and Giaccia, A.J. "Radiobiology for the Radiologist", seventh edition. Philadelphia, PA: Lippincott Williams & Wilkins; 2012.

Health threat from cosmic rays, 2015. Available at: https://www.revolvy.com/topic/Health%20threat%20from%20cosmic%20rays&item. Accessed 17 September 2017.

ICRU, International Commission on Radiation Units and Measurements. Linear Energy Transfer. Washington, D.C. ICRU Report 16; 1970.

ICRU, International Commission on Radiation Units and Measurements. Average energy required to produce an ion pair. Bethesda, Maryland. ICRU Report 31; 1979.

ICRU, International Commission on Radiation Units and Measurements. Microdosimetry. Bethesda, Maryland. ICRU Report 36; 1983.

ICRU, International Commission on Radiation Units and Measurements. Quality factor in radiation protection. Bethesda, Maryland. ICRU Report 40; 1986.

Kellerer, A.M. "Microdosimetry: Reflection on Harald Rossi", Radiation Protection Dosimetry, Vol. 99, pp 18-22; 2002.

Knoll, Glenn F., "Radiation Detection and Measurement", fourth edition. Hoboken, NJ: Wiley & Sons; 2010.

Los Alamos National Laboratory. "Monte Carlo Methods, Codes, and Applications Group". Available at: https://mcnp.lanl.gov/. Accessed 21 September 2017.

Miroshnichenko, Leonty I, "Radiation Hazard in Space". Dordrecht, The Netherlands: Kluwer Academic Publishers; 2003.

Moro, D., Chiriotti, S., Colautti, P., and Conte, V. "TEPC Gas Gain measurements in Propane". Radiation Protection Dosimetry, Vol 161, No. 1-4, pp. 459-463; 2014.

NASA, "NASA Space flight Human-System Standard 3001, Volume 1, Revision A: Crew Health." National Aeronautics and Space Administration. Washington D.C; 2015.

NASA Glenn Research Center, "Gas Pressure", National Aeronautics and Space Administration, 2015. Available at: https://www.grc.nasa.gov/WWW/K-12/airplane/pressure.html Accessed 14 October 2017.

National Research Council, "Managing Space Radiation Risk in the New Era of Space Exploration", National Academy of Science. Washington D.C; 2008.

Oak Ridge National Laboratory. "MCNP6 User's Manual Code version 6.1.1". Los Alamos National Laboratory report LA-CP-14-00745, June 2014.

O'Neill, P.M., Golge, S., Slaba, T.C. "Badhwar-O"Neill 2014 Galactic Cosmic Ray Flux Model Description". National Aeronautics and Space Administration, Johnson Space Center. Houston, Texas; 2015.

Paul, H. "Stopping Power of Matter for Ions". International Atomic Energy Agency, 2015. Available at: https://www-nds.iaea.org/stopping/. Accessed 20 September 2017.

Perez-Nunez, D. "Design, Construction, and Implementation of Spherical Tissue Equivalent Proportional Counter". PhD Dissertation. Texas A&M University; 2008.

Perez-Nunez, D. and Braby, L.A. "Replacement Tissue-Equivalent Proportional Counter for the International Space Station", Radiation Protection Dosimetry, Vol. 143, pp. 394-397; 2011.

Riman, F.M., "Tissue Equivalent Proportional Counter (TEPC)", International Space Station, National Aeronautics and Space Administration, 2012. Available at: https://www.nasa.gov/mission_pages/station/research/experiments/TEPC.html. Accessed 3 December 2017.

Rossi, H.H. and Zaider, M. "Microdosimetry and its applications" New York: Springer; 1996.

Saha, G.B. "Gas-filled Detectors". Physics and Radiobiology of Nuclear Medicine. New York: Springer; 2012.

Straume, T., Braby, L.A., Borak, T.B., Lusby, T., Warner, D.W., and Perez-Nunez, D. "Compact Tissue-Equivalent Proportional Counter for Deep Space Human Missions". Health Physics Society, Volume 109, Number 4; 2015.

APPENDIX

SAMPLE MCNP6 INPUT DECKS

```
C  Cell Card 3.8 cm for protons
1 10 -0.000053   -3                  imp:h=1    $Propane inside sphere
2 20 -1.127       3 -2               imp:h=1    $A-150 wall
3 0               2 -1               imp:h=1    $void
4 0               1                  imp:h=0

C Surface Card
1 SO 3.0
2 SO 2.4                                        $A-150 shell
3 SO 1.9                                        $Inside Sphere

C Mode Card
mode H
PHYS:H 1800
SDEF SUR=1 NRM=-1 ERG=1000 PAR=H
F8:H 1
E8 0 .0001 10i .001 10i .01 10i .1 10i 1.0 10i 2.0
C Material identification
m10     6000   -0.2727                  $Propane
          1001  -0.7273
m20     1001   -0.102                   $A-150 plastic shell
          6000  -0.768
          8016   -0.0590
          7014   -0.036
          20000 -0.018
          9019   -0.017
NPS 1000000
```

```
C  Cell Card 1.8 cm for protons
1 10 -0.00011     -3                  imp:h=1    $Propane inside sphere
2 20 -1.127        3 -2               imp:h=1    $A-150 wall
3 0                2 -1               imp:h=1    $void
4 0                1                  imp:h=0

C Surface Card
1 SO 2.0
2 SO 1.2                                         $A-150 shell
3 SO 0.9                                         $Inside Sphere

C Mode Card
mode H
PHYS:H 1800
SDEF SUR=1 NRM=-1 ERG=1000 PAR=H
F8:H 1
E8 0 .0001 10i .001 10i .01 10i .1 10i 1.0 10i 2.0
C Material identification
m10     6000   -0.2727                           $Propane
         1001  -0.7273
m20     1001   -0.102                            $A-150 plastic shell
         6000  -0.768
        8016   -0.0590
        7014   -0.036
        20000 -0.018
        9019   -0.017
NPS 1000000
```